

Organic cations in halide perovskite solid solutions: exploring beyond size effects

F. B. Minussi^{1*}, R. M. Silva Jr.², J. C. S. Moraes¹, E. B. Araújo¹

¹ Department of Physics and Chemistry, São Paulo State University, 15385-007, Ilha Solteira, SP - Brazil

² Department of Electrical Engineering, São Paulo State University, 15385-007, Ilha Solteira, SP - Brazil

Abstract

Halide perovskites are a class of materials of consolidated optoelectronic and electrochemical applications, reaching efficiencies compared to established materials in respective fields. In this scenario, the design and understanding of composition-structure-property relations is imperative. In solid solutions containing mixed cations, some direct relations between the sizes of the substituents and the properties of perovskites are generally observed. However, in several cases, these relations are not observed, implying that other characteristics of these cations play a major role. Despite its importance, this understanding has not been comprehensively deepened. To address this issue, we synthesized and characterized the structure, electrical behavior, and stability of methylammonium lead iodide-based perovskites with equal amounts of the substituents guanidinium, ethylammonium, and acetamidinium. These three large organic cations have essentially equal sizes but other remarkably different characteristics, such as the number of N-H bonds, intrinsic dipole moment, and order of C-N bonds. Herein, we show that these cations have dramatically different effects over important fundamental and applied properties of resulting perovskites, including the orthorhombic-to-tetragonal and tetragonal-to-cubic phase transitions, microstructural development, ionic conductivity, I-V hysteresis, electronic carrier mobility, and stability against light-induced degradation. These effects are correlated with the characteristics of the large substituent cations and help pave the way for a better rational chemical design of halide perovskites.

Keywords: Halide perovskites; Methylammonium; Guanidinium; Ethylammonium; Acetamidinium.

* corresponding author: fbminussi@gmail.com

1. INTRODUCTION

Halide perovskites are compounds with the general ABX_3 composition, where A represents a monovalent cation, B a divalent cation, and X a halide anion, constructed by a tridimensional arrangement of corner-sharing BX_6 octahedra [1]. This class of materials has recognized diverse optoelectronic applications owing to their chemical, structural, synthetic, and property vastness [2-10]. With intense initial progress and current establishment of the fundamentals of these materials, with high efficiencies being obtained in perovskite devices, as in solar cells [11], these materials can be close to the commercial outbreak as their main bottleneck, i.e., their instability issues, keeps getting better addressed [12-17]. In this scenario of technological maturity, a great part of the scientific challenges ahead lies in consolidating the understanding of the principles behind empirical knowledge about these materials. These same concerns were pointed out recently regarding the photo-stability of halide perovskites [18].

Formulating solid solutions for mixed cations at the A-site is one of the relevant strategies for obtaining the desired set of characteristics in halide perovskites [19,20,21]. In fact, most top-efficiency devices fabricated with halide perovskites use mixed cation compositions [22]. In these A-site mixed compositions, a plethora of cations can be used, including inorganic potassium (K^+), rubidium (Rb^+), and cesium (Cs^+), as well as organic such as methylammonium (MA^+), formamidinium (FA^+), imidazolium (IM^+), methylhydrazinium (MHy^+), aziridinium (AZi^+), azetidinium (AZe^+), dimethylammonium (DMA^+), ethylammonium (EA^+), acetamidinium (AC^+), and guanidinium (GA^+) [23-27]. General rules of thumb for the formation of stable tridimensional halide perovskites are choosing compositions with a Goldschmidt tolerance factor between 0.8 and 1.0 [28,29] or a Bartel tolerance factor below 4.18 [30], both of which are essentially determined by the sizes of the ions involved. Not surprisingly, it is well-known that the sizes of the A-site cations dramatically affect the halide perovskites' properties [23,31-36]. For example, it was found that increasing the size of substituent cations in perovskites based on methylammonium lead iodide ($MAPbI_3$) decreases ionic conductivity and increases the activation energies [37]. The main differentiating factor for inorganic cations used in halide perovskites is often associated with their ionic radii. However, in the organic cations used in halide perovskites, characteristics other than size are of great relevance, such as chemical composition, existence of double bonds, possibility of formation of hydrogen bonds,

shape, and polarity. In this sense, it is recognized that aspects beyond the size of the substituent cations can affect the properties of the resulting materials [23].

In recent work, it was shown that the formation of single-phase solid solutions of halide perovskites in compositions of the type $A_xMA_{1-x}PbI_3$ is also strongly dependent on the number of N-H bonds of the substituent A^+ cations [38]. In terms of their properties, it was suggested that the formation of hydrogen bonds, also related to the N-H bonds of organic cations, is a factor responsible for the increase in stability in the $AC_xMA_{1-x}PbI_3$ system, given that the AC^+ cations have four N-H bonds, while MA^+ has only three [39]. However, it was shown that $GA_xMA_{1-x}PbI_3$ compositions can have lower thermal stabilities than pure $MAPbI_3$, although GA^+ has six N-H bonds [40,41]. Furthermore, it has recently been shown that other properties of interest in halide perovskites, for example, permittivities and phase transitions in $GA_xFA_yMA_{1-x-y}PbI_3$ compositions, are also not dependent solely on the size of the substituent cations [42]. Concerning phase transitions, expectations based on the size of the substituents would suggest that the $GA_xMA_{1-x}PbI_3$ system would have transition temperatures between tetragonal and cubic symmetries lower than those of the $FA_xMA_{1-x}PbI_3$ system, given that the GA^+ cations are considerably larger than FA^+ , but it is experimentally observed the opposite [40,42]. In low-temperature transitions, it has been shown that stabilizing other symmetries may depend on factors such as size, number of N-H bonds, and dipoles of the substituent cations [42]. Phase transitions in halide perovskites are relevant for optoelectronic applications and were the subject of a recent high-impact review [43]. On its side, the cation dipoles in halide perovskites are reported to influence several factors, such as charge separation, electronic energy states, phase transitions, defect structure, ion transport, and formation of ferroic domains [44-47]. For example, compared to $FA_xMA_{1-x}PbI_3$ and $GA_xMA_{1-x}PbI_3$ [42], $EA_xMA_{1-x}PbI_3$ compositions apparently have higher dielectric permittivities [48], which may be due to the fact that the intrinsic dipole magnitude of EA^+ cations is higher than that of FA^+ and GA^+ .

Given the above-depicted scenario, the present work reports the synthesis of $MAPbI_3$ -based solid solutions containing equal amounts of substituent cations of nearly equal sizes, namely GA^+ , EA^+ , and AC^+ . By comparing the structure, electrical behavior, and stability of $MAPbI_3$, $GA_{0.1}MA_{0.9}PbI_3$, $EA_{0.1}MA_{0.9}PbI_3$, and $AC_{0.1}MA_{0.9}PbI_3$ perovskites, it was possible to mitigate the effect of the substituent size to verify how the other characteristics of these substituent cations, mainly the number of N-H bonds and the intrinsic dipole moment, can alter the properties of the perovskites. The results show

that despite having similar sizes, these cations lead to dramatically different behavior in the characteristics of resulting materials. These results advance the knowledge of the effects of different A-site substituent cations on the properties of halide perovskite solid solutions.

2. EXPERIMENTAL

2.1 Sample synthesis

For the present study, samples of the four halide perovskites of compositions MAPbI_3 (or MAPI), $\text{GA}_{0.1}\text{MA}_{0.9}\text{PbI}_3$ (or GA0.1), $\text{EA}_{0.1}\text{MA}_{0.9}\text{PbI}_3$ (or EA0.1), and $\text{AC}_{0.1}\text{MA}_{0.9}\text{PbI}_3$ (or AC0.1) were prepared from the precursors lead iodide (PbI_2 , Sigma-Aldrich, 99 %), methylammonium iodide (MAI, Sigma-Aldrich, 99 %), guanidinium iodide (GAI, Sigma-Aldrich, 99 %), ethylammonium iodide (EAI, Sigma-Aldrich, 99 %), and acetamidinium iodide (ACI, Sigma-Aldrich, 98 %). A total of approximately 1.2 g of precursors (Supplementary Note 1) were mixed and ground to mechanochemically react in a hermetic 25 ml polytetrafluorethylene vessel filled with about 40 % volume of zirconia balls of diameters between 2 and 6 mm. The system was gently hand-shaken for about 40 minutes. The resulting black powders of perovskites were sieved in a 250 μm aperture sieve (60 mesh), and dried and annealed for 3 hours at 70 °C in a laboratory oven with periodic (once every 30 minutes) stirring. Pelletized powders were produced with 150 ± 5 mg of the powders uniformly spread into a 10 mm diameter circular cavity of a metallic mold and compacted with a pressure of about 250 MPa. Lastly, the pellets were sintered in an electric furnace at 120 °C for 3 hours and slowly cooled to room temperature inside the electric furnace. Several pellets of each composition were synthesized and used in the present study.

2.2 Characterizations

The crystalline structure of the materials was characterized by X-ray diffraction (XRD) using a Rigaku Ultima IV diffractometer with $\text{CuK}_{\alpha 1}$ radiation ($\lambda = 1.5406 \text{ \AA}$), under 40 kV and 20 mA, with a continuous scan (2° min^{-1}), under dark and at about 25 °C in the range of 2θ from 10 to 50°. Differential scanning calorimetry (DSC) measurements were performed in a DSC 25 - TA Instruments from -50 to 100 °C, with a $5^\circ \text{ C min}^{-1}$ heating rate, under a nitrogen atmosphere, using about 10 to 15 mg of pellets fragments in hermetically closed aluminum crucibles. The microstructure images of the samples were obtained in a Zeiss EVO LS15 scanning electron microscope (SEM), with

a tungsten beam operating in the voltage range between 10 and 20 kV, by secondary electron analysis. Fourier transform infrared spectroscopy (FTIR) was performed on a Nicolet NEXUS 670, with 256 scans, resolution 4, sample gain 8, from 600 to 2000 cm^{-1} , using the specular reflection mode with sintered samples, at room temperature (~ 25 $^{\circ}\text{C}$).

For electrical measurements, circular gold electrodes of about 0.6 mm diameter were sputtered on top of the perovskite pellets using a copper shadow mask, while a bottom gold electrode was deposited over the entire sample surface. Impedance spectroscopy (IS) measurements were performed in a Displex ARS CSW-202 closed system using an Agilent 4284A LCR meter to measure the conductance (G) and susceptance (B) in the frequency range of 5.10^3 to 10^6 Hz. Room temperature IS measurements were conducted in the dark. Data were collected on cooling and heating regimes at 1 $^{\circ}\text{C min}^{-1}$ in the -173 to 27 $^{\circ}\text{C}$ range using vacuum and dark conditions for temperature-dependent dielectric permittivity analyses. Before starting measurements under heating, the samples were kept at -173 $^{\circ}\text{C}$ for 30 minutes. Several electrodes were systematically tested before starting the experiment, and impedance spectra were collected to ensure the choice of a representative electrode of the overall sample's electrical characteristics. Steady-state current-voltage (I - V) data were collected using a Keithley 6517B electrometer in the dark at room temperature. Cycle up and down measurements were performed from -6 to $+6$ V with a 0.1 V s^{-1} scan rate. Forward measurements were performed from 0 to $+20$ V with a scan rate of 0.5 V s^{-1} .

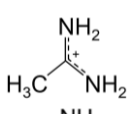
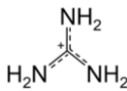
2.3 Light-accelerated degradation tests

For degradation experiments, pellets were placed in a 60 x 15 mm glass Petri dish and submitted to constant illumination for up to 120 h in a homemade closed setup (Supplementary Note 2). Throughout the experiment, temperature and relative humidity ranged from 25 to 32 $^{\circ}\text{C}$ and 45 to 55 %, respectively. After predefined intervals, the samples were removed from the setup, and XRD data were collected using the same operational conditions described earlier but in the 2θ range from 10 to 35° . Precautions were taken so that the same faces of the samples were exposed to the illumination during the test. The XRD data were collected on those same faces, with meticulous care taken to position the samples in the same arrangement in the sample holder throughout the experiment. After the 120 h test period, SEM images were also obtained.

3. RESULTS AND DISCUSSION

Before discussing the properties of synthesized perovskites, it is convenient to briefly establish the differences between the host methylammonium cations and the studied substituent cations. As is shown in Table 1, considering early estimations [28,29], EA⁺, AC⁺, and GA⁺ cations are quite larger than MA⁺, but have themselves essentially the same effective ionic radius (r_{eff}). Although this consideration is made, and even though these values have been widely used in the literature, it must be kept in mind that, especially when it comes to molecular ions, the effective ionic radii of chemical species are not exact values and should be distributed over a more or less wide range of values, which are difficult to determine [49]. That said, even if the herein used large cations do not have the same radii, the differences should not be large enough to affect the results appreciably, as the other differences are possibly more relevant. Similar to MA⁺, EA⁺ is also a linear cation with no unsaturated bonds and with the same number of N-H bonds (n_{NH}), but much more polar as given by their intrinsic dipole moments (d). On the other hand, both acetamidinium and guanidinium cations are planar. Acetamidinium is slightly less polar than MA⁺, possesses four N-H bonds and has one delocalized double bond, existing as two resonance hybrids (order of C-N bond is 1.5), while guanidinium is non-polar, has six N-H bonds, also possesses one delocalized double bond, and exists as three resonance hybrids (order of C-N bond is 1.33).

Table 1 - Summary of main characteristics of the A-site organic cations used in this work. r_{eff} , n_{NH} , and d are, respectively, the effective ionic radius (values taken from [28] and [39]), number of N-H bonds, and intrinsic dipole moment (values estimated using MolCalc [50]).

Cation	Symbol	Structure	r_{eff} (pm)	n_{NH}	d (D)
methylammonium	MA ⁺	$\text{H}_3\text{C}-\overset{+}{\text{N}}\text{H}_3$	217	3	2.69
ethylammonium	EA ⁺	$\text{H}_3\text{C}-\text{H}_2\text{C}-\overset{+}{\text{N}}\text{H}_3$	274	3	4.97
acetamidinium	AC ⁺		277	4	2.01
guanidinium	GA ⁺		278	6	0

The crystalline structure of the perovskites was studied considering the basic information on the important organic cation setup and the X-ray diffraction data. The results are summarized in Figure 1a. The first aspect to be mentioned is the formation of

the perovskite phase with the peaks assigned in the expected 2θ positions and with high phase purity. Typical non-perovskite APbI_3 ($\text{A}^+ = \text{GA}^+, \text{EA}^+, \text{AC}^+$) [39,48,51] or unreacted PbI_2 secondary phases that could appear, which intense peaks appear, respectively, at 2θ values of about 11.0 and 12.5° , are not identified in the diffractograms of any composition. That means that the formation of perovskites proceeded with a high reaction extent between the precursors and that the mixed-cation compositions have substituent contents below the solubility limit, as expected from literature data [38].

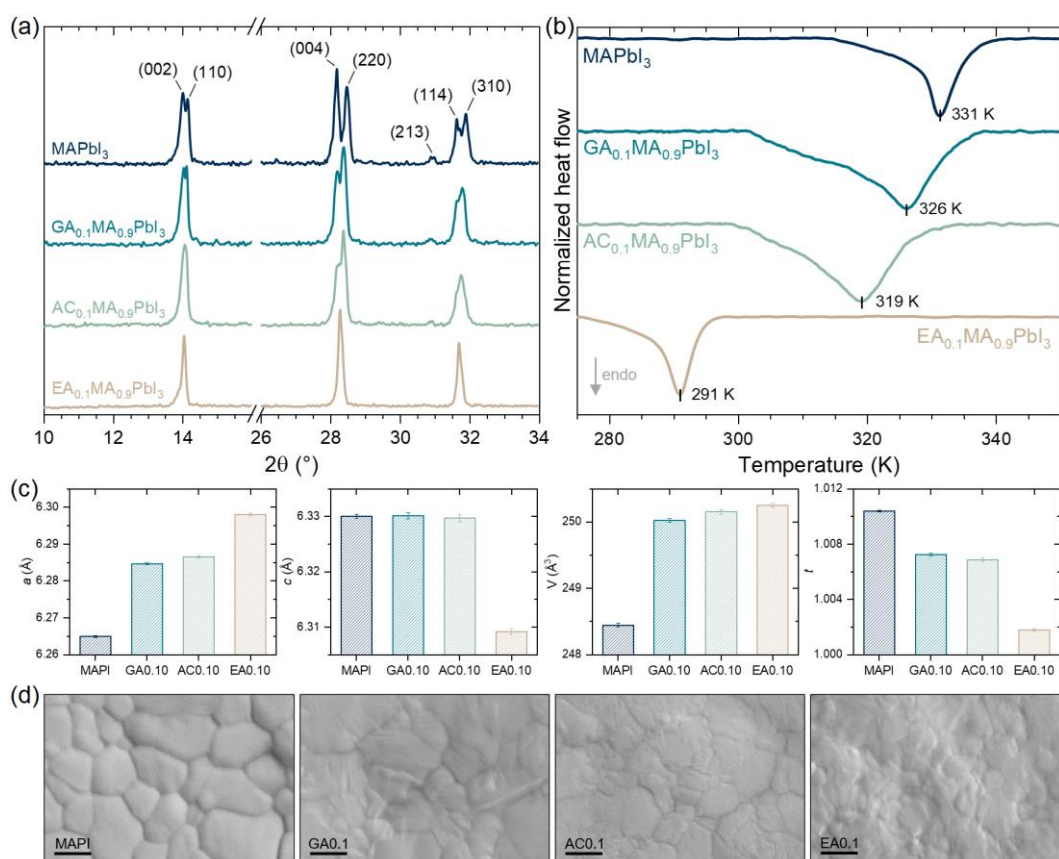


Figure 1 - (a) X-ray diffraction patterns of the studied compositions. Only the 2θ intervals of main peaks are shown. (b) DSC thermograms obtained on heating regimes. (c) Lattice parameters a and c , cell volume V , and tetragonality factor $t = c/a$. The parameters shown were calculated using the relations $a = a'/\sqrt{2}$ and $c = c'/2$ of a pseudocubic representation, where a' and c' are the parameters obtained through the Le Bail fit of XRD data using the $I4cm$ space group. Error bars are the fit residuals. (d) SEM images of the studied compositions. Scale bars are $1 \mu\text{m}$.

Another important regarding the XRD results is the increased superposition of peaks due to reflection by planes (002) and (110) at $\sim 14.0^\circ$, (004) and (220) at $\sim 28.2^\circ$, and (114) and (310) at $\sim 31.8^\circ$ for the perovskite solid solutions compared to MAPbI_3 . Furthermore, the intensity of the peak related to the reflection of plane (213) at $\sim 31.5^\circ$ lowers while the peaks mentioned above get more superposed. It is well known that

MAPbI₃ is tetragonal (space group *I4/mcm* or *I4cm*, depending on the reference [52,53]) at room temperature and transitions to cubic (space group *Pm $\bar{3}$ m* [54,55]) symmetry (T → C) at ~ 60 °C [54,56]. The existence of separated above peaks and the presence of the (213) peak are signatures of the tetragonal phase. The fact that the solid solutions display increased superpositions and progressive vanishing of (213) peak means that the structures of the perovskites are “less tetragonal” at the measured temperature, i.e., that the sizes of the lattice parameters *a* and *c* are closer and possibly have lower T → C transition temperatures. In this sense, the analysis of diffractograms suggests the T → C temperature of the studied solid solutions decreases in the order GA_{0.1} > AC_{0.1} > EA_{0.1}. To confirm this trend, we performed DSC measurements. The results are shown in Figure 1b. The trend was confirmed by considering the maximum values of the endothermic peaks.

We recently observed that GA⁺-rich compositions possess higher T → C transition temperatures than FA⁺-rich compositions in the GA_xFA_yMA_{1-x-y}PbI₃ system [42]. Since entropic factors arriving from the mixing of A-site cations and cation dynamics are of crucial importance in stabilizing the cubic phase of HPs [23,57,58,59], we proposed that the number of N-H bonds may play an important role. With more N-H bonds, it is likely that the cations are more restricted due to the formation of hydrogen bond interactions with the iodide anions. In this sense, the GA⁺ cations, with six N-H bonds, would contribute less to the rotational entropy of the system than the FA⁺ cations, which have only four N-H bonds. Also, distortions induced by the formation of such hydrogen bonds would make it more difficult for the lattice to achieve the non-tilted arrangement of the PbI₆ octahedra of the cubic phase. Based on this rationale, we inferred that EA⁺ cations, with three N-H bonds, would be more effective in stabilizing the cubic phase, confirmed experimentally by the comparison with literature data [48]. Now, extending the approach, the trend of the T → C temperature again suggests a correlation between the number of N-H bonds and the transition temperature. It is also interesting to note that the T → C temperature order is inversely proportional to the intrinsic dipole moment of the substituents. It is known that the cation dynamics, or dipole dynamics, play a crucial role in the structure and phase transitions of hybrid halide perovskites [60]. However, the effect of the dipole magnitude on the T → C transition remains without deep exploration. In principle, the magnitude of the dipoles would increase the interactions between neighboring cations and thus the tendency of dipole ordering, hindering the rotational

freedom of the cations. Consequently, this possibility would be the increase in the T → C transition temperature, which is the opposite behavior observed here, suggesting that the effect of the dipole magnitude may not be obvious and has to be better addressed in future endeavors. An important conclusion from these analyses is that cations of the same size may have dramatically different effects on the phase stability of solid solutions.

One consequence of the different large cations is their effects on the crystal parameters, given in Figure 1c. To obtain the parameters, we performed Le Bail fits of XRD data using the *I4cm* space group (details in Supplementary Note 3). While lattice parameter *a* increases in the same trend of cubic phase stabilization, lattice parameter *c* are essentially the same for MAPbI₃, GA0.1, and AC0.1, but remarkably lower for EA0.1. These results indicate a somewhat higher degree of A-site cations directionality perpendicular to z-axis. Despite that, the cell volume of solid solutions is essentially the same considering the error bars, consistent with the sizes of substituent cations being very close. Lastly, the tetragonality factor ($t = c/a$) decreases in the same trend of the T → C temperature, as expected, reflecting the higher superposition of XRD peaks discussed above. From the microstructure perspective, as seen in SEM images in Figure 1d, all studied compositions show quite dense microstructures, without secondary phases and with clearly distinctive grains and grain boundaries in MAPbI₃ compared to the other compositions. Since microstructure development involves the diffusion of ions, this observation suggests that migration of ions is hindered in A-site solid solutions, which is consistent with the general literature consensus [61,62,63]. For GA_xFA_xMA_{1-2x}PbI₃, a correlation between ion transport and microstructural development in perovskites was proposed [64]. Experimental data in this regard will be later discussed.

FTIR spectra were also obtained to acquire more information regarding the properties of the organic cations within the perovskite structure. The spectra and information of the bands of interest are provided in Figure 2 and Table 2, respectively. Emphasis is placed on the low wavenumber region (700 to 1800 cm⁻¹), in which intense bands related to C-N and N-H bonds are present with less humidity interference. The direct comparison between the full-range spectra in Figure 2a shows that all peaks observed in the precursor methylammonium iodide are also observed in the MAPbI₃-based materials. This is unsurprising since the MAI peaks are due to vibrations of the MA⁺ cation, which are present in all other compositions. On the other hand, peak positions and relative intensities vary considerably. For a better visualization, we separated the spectra in upper and lower wavenumber regions of the studied range, as

shown in Figure 2b. The first important observation is the obvious shift of all MA⁺ peaks (modes assigned as ν_1 , ν_2 , and ν_3) to lower wavenumber from MAI to the perovskites, owing to their distinctive chemical and structural differences, which affects local polarizability and hydrogen bond capabilities [65]. Second, for the perovskites of different compositions, there seems to be little effect of the substituent cations in the MA⁺ vibrational modes. Perhaps the substituting degree is not high enough for subtle differences to be detected under the definition of the employed operational conditions. Despite that, it is intriguing that for modes ν_1 and ν_3 , directly related to -NH₃⁺ group, the effects of substitution with GA⁺ and EA⁺ appear to be opposite, where GA⁺ increases the wavenumbers while EA⁺ reduces them. These two cations have the lowest and highest intrinsic dipole moments among the studied cations. In principle, this can be related to the higher local polarizability of EA0.1 compared to MAPbI₃, which tends to decrease the local fields and, consequently, the resonance frequency (or its wavenumber) of the vibrational excitations [65]. On the contrary, with null dipole moment, GA⁺ cations would tend to result in a less polarized medium, increasing the wavenumber of observed peaks. Based on an inductive effect, this effect can also be understood, where non-polar GA⁺ cations polarized the medium and, therefore, the structure composed of PbI₆ octahedra will have less displacement of its electronic clouds [64]. Therefore, when the inductive effect is reduced, the electronic clouds in organic cations will also be less displaced, which should increase the charge density in the chemical atmosphere around the bonds present in the MA⁺ cations, increasing the intensity of the bonds. The correlation between the wavenumber ($\bar{\nu}$) of a band and the chemical bond strength can be qualitatively assessed from the harmonic oscillator equation given by $\bar{\nu} = (1/2\pi c) \cdot (\sqrt{K/\mu})$, where K is the “force constant” of a bond and μ is the reduced mass of the bound atoms [66]. Again, for the EA⁺ cations, the effect would be the exact opposite as their dipole moment is higher than that of MA⁺. Before anything else, we emphasize that interesting discussions require more data with high-resolution FTIR and related techniques for more enlightening results and interpretations. That being said, the modes assigned as ν_4 and ν_5 , due to C-N bond stretching in GA⁺ and AC⁺ cations, respectively, do differ strongly from each other, and the C-N bond stretching of MA⁺ cations, assigned as ν_2 . The wavenumbers increase in the order from MA⁺ < GA⁺ < AC⁺ due to the increased bond order in the same trend, as depicted in the harmonic oscillator equation.

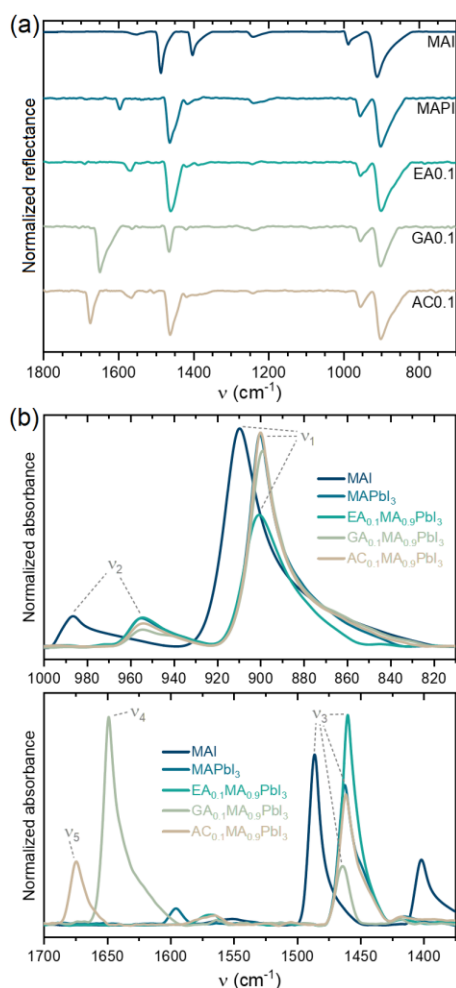


Figure 2 - (a) Normalized reflectance and (b) absorbance spectra at lower (top) and higher (bottom) wavenumbers obtained by FTIR for the studied compositions. The experimental spectra of the MAI precursor used in this work are also presented for better comparison. The unassigned bands are due to C-C, C-H, O-H bonds or coupled modes of no analytical use in this work.

Table 2 - Characteristics of assigned bands in FTIR spectra. All values in cm^{-1} . Wavenumber imprecisions are of $\pm 1 \text{ cm}^{-1}$. (-): non-existent bands. (*): The peaks are possibly superpositions of the same MA^+ and EA^+ cations vibration modes.

Band	Attribution	Cation	MAI	MAPI	EA0.1*	GA0.1	AC0.1
ν_1	$\text{CH}_3\text{-NH}_3^+$ rocking	MA^+	910	900	899	901	900
ν_2	C-N stretching	MA^+	987	955	955	955	954
ν_3	NH_3^+ sym. bending	MA^+	1486	1463	1460	1464	1462
ν_4	C-N stretching	GA^+	-	-	-	1649	-
ν_5	C-N stretching	AC^+	-	-	-	-	1674

To study the effects of different substituent cations on the phase transitions of the MAPbI_3 -based perovskites at lower temperatures, impedance spectroscopy measurements were also performed, focusing on the real (ϵ') and imaginary (ϵ'')

dielectric permittivity. Figure 3 shows their dependencies on temperature at 1 MHz, obtained under heating and cooling regimes. This frequency was chosen to diminish the contribution of extrinsic polarization mechanisms.

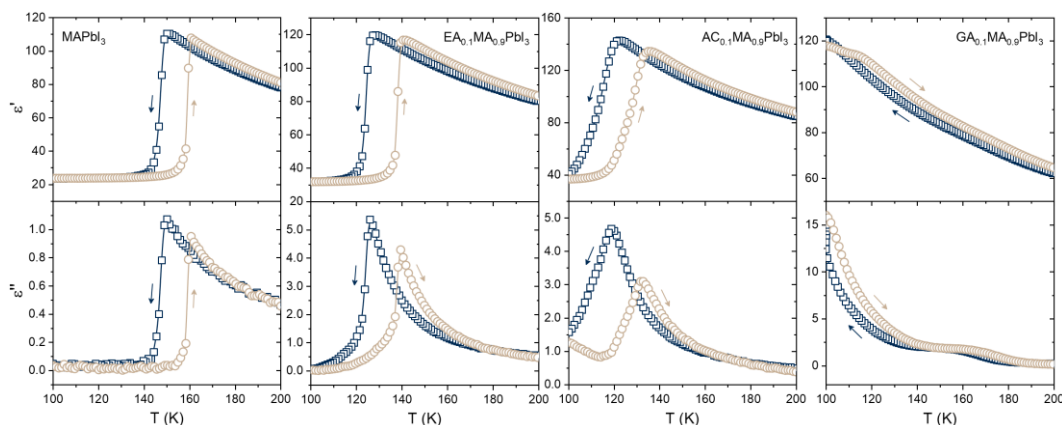


Figure 3 - Temperature dependencies of the real (ϵ') and imaginary (ϵ'') components of the dielectric permittivity at 1 MHz measured on cooling (blue) and heating (gray)

In MAPbI₃, from the heating curves perspective, the abrupt change on both ϵ' and ϵ'' at about 160 K (-113 °C) marks the orthorhombic-to-tetragonal phase transition (O → T) [67,68]. In the orthorhombic phase (space group *Pnma* [55]), MA⁺ cations are fully ordered [69,70,71] and frozen in fixed directions [72]. With increasing temperature, the sudden increase in the dielectric permittivity is due to disrupting the cooperative ordering of MA⁺ cations [48,73] to a state of partial disorder in the tetragonal phase [69,70]. In FA_xMA_{1-x}PbI₃ perovskites, several different phases may exist in low temperatures [74,75], which, in conjunction with dielectric measurements in GA_xFA_yMA_{1-x-y}PbI₃ perovskites [40,42], led to the inference that, on heating, the disappearance of the orthorhombic phase is accompanied by a peak in the ϵ'' curve, while the appearance of the tetragonal phase is accompanied by a rapid increase in ϵ' . From that perspective, the studied solid solutions have lower O → T transition temperature than MAPbI₃, possibly with no other stable phases in the studied range. On heating, for EA0.1, the O → T transition occurs at about 140 K (-133 °C), at 133 K (-140 °C) for AC0.1, and below 100 K (-173 °C) for GA0.1. With that in mind, there seems to be a direct correlation between the transition temperature and the electric dipole of the substituents, an inverse correlation with their number of N-H bonds, or both. However, experimental results in FA_xMA_{1-x}PbI₃ and GA_xFA_yMA_{1-x-y}PbI₃ perovskites show that high FA⁺-contents may lead to an increase in the temperature demanded for the perovskite to be a tetragonal single phase compared

to MAPbI₃ [42,74]. Taking aside that FA⁺ cations are smaller than those used in this work, it has four N-H bonds and is close to the null electric moment. Hence, this behavior doesn't fit the above-suggested correlations. In this scenario, having in mind that several different and connected effects are expected to play a role, including steric hindrance of rotational motion, dipole-dipole interactions, hydrogen bonds, and inorganic cage deformation [29,46,76], we have already pointed out that the relation between the O → T transition in solid solutions and the characteristics of substituents is an intricate combination of cation sizes, dipoles, and number of N-H bonds [42]. Present experimental results reinforce this intricacy. A better elucidation of these correlations could be achieved through more data being obtained in other MAPbI₃-based solid solutions in conjunction with actual crystallographic data that allows the exact stable phases that may coexist at low temperatures. Such data would also be valuable to access the nature of the subtle shoulder present in ϵ'' at ~160 K for the GA0.1. This type of signal appears consistently in GA_xMA_{1-x}PbI₃ and GA⁺-rich GA_xFA_yMA_{1-x-y}PbI₃ compositions [40,42], which leads to the conclusion that it is not an experimental artifact. Lastly, we mention that along the tetragonal phase, the progressive decay of ϵ' with temperature means that the temperature dependence of the dielectric permittivity is dominated by dipolar polarization, whose contribution diminishes through thermal randomization by increasingly free dipole rotation with temperature. Since this occurs for all the studied compositions, we infer that the differences observed in their dielectric behavior are mostly due to changes related to how the substituent cations affect the dynamics of MA⁺ cations rather than the behavior of the substituent cations themselves, in line with previous interpretations [42].

As halide perovskites are vastly meant for optoelectronic and electrochemical devices, it is imperative to understand their electrical behavior. In this sense, we evaluated the charge transport characteristics of the studied compositions by impedance spectroscopy and steady-state current-voltage measurements at room temperature. The results are shown in Figure 4. From IS measurements, the collected frequency-dependent data was converted to the real (Z') and imaginary (Z'') components of the dielectric. In Figure 4a, the so-called Nyquist plots of Z'' vs Z' impedance arcs are shown. In these plots, it is well known that the diameter of the arcs is proportional to the resistance (R) of the samples. Hence, there seems to be a trend of increasing the sample resistance such that MAPI < GA0.1 < EA0.1 < AC0.1. The Nyquist plots were modeled using the Cole-Cole relaxation model [77] to obtain the resistances, where it is assumed the sample can

be treated as a parallel association of a resistor of resistance R and a constant phase element (CPE) to account for the distribution of relaxation times. In this case, the fitting equation is given by $Z'' = \sqrt{[(R/2)\text{cosec}(\varphi)]^2 - [Z' - R/2]^2} - (R/2)\cot g(\varphi)$, where $\varphi = b\pi/2$ and b is the Cole-Cole coefficient, an empirical parameter, in the interval between 0 and 1, which reflects the existence of a distribution of relaxation times in the material and deviation from the ideal Debye relaxation. A detailed derivation of the above equation can be found elsewhere [51]. Then, the obtained resistances were converted to the conductivity (σ_{dc}) of the materials using the relation $\sigma_{dc} = L/AR$, where L is the distance between the electrical contacts (i.e., the sample thickness of about 500 μm as given in Supplementary Note 4) and A is the electrode area ($\sim 3.10^{-7} \text{ m}^2$). The results are shown in Figure 4b. As expected, the conductivity of the materials followed the same trend as the sample's resistances.

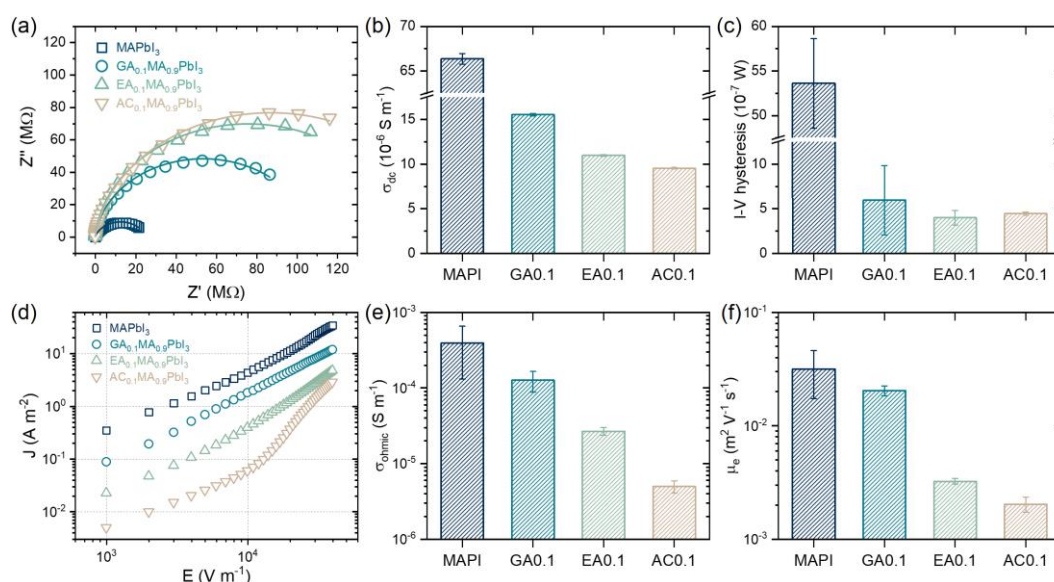


Figure 4 - (a) Impedance Nyquist plots of studied materials. Symbols are the experimental data and lines that fit the Z'' vs Z' the equation derived from the $R|CPE$ model. (b) Conductivity values are calculated from the extracted resistances. (c) I - V hysteresis determined using current-voltage cycles in the -6 to $+6$ V and a 0.1 V s^{-1} scan rate. (d) Forward J - E data was obtained using current-voltage measurements from 0 to $+20$ V and 0.5 V s^{-1} scan rate. The curves shown are the mean of four measurements. (e) Ohmic conductivity is determined from J - E curves at low electric fields. (f) Electronic charge carrier mobility was estimated using the models described in the main text. Except for σ_{dc} , errors bars are the standard deviation from the mean. For σ_{dc} , error bars are the fit residuals.

Increasing experimental evidence demonstrates that the electrical response measured by impedance spectroscopy in halide perovskites is controlled by mobile ions

[78,79,80], which, in MAPbI₃-based materials, are mostly iodine vacancies and interstitials [81,82,83]. With that in mind, results suggest that the solid solution's ionic transport is strongly mitigated compared to MAPbI₃, as pointed out previously. However, the difference is that EA⁺ and AC⁺ seem more effective than GA⁺ in reducing the transport of ions. From the mechanical perspective of a bowed path of ions during charge transport [37], we interpret these results based on the fact that during the jump between two locally stable sites, the iodine ions are subjected to higher repulsion/attraction electrostatic interactions with the EA⁺ and AC⁺ cations of higher dipole moments compared to the non-polar GA⁺ cations, hindering their transport and diminishing the materials' conductivity. This corroborates the findings that the activation energy for ion movement increases with the magnitude of the A-cation dipole [47]. Noteworthy, mitigating the ion transport in the solid solutions may explain the slower microstructural development earlier observed. Since ionic conductivity (σ) and diffusivity (D) are connected by the Nernst-Einstein equation, given by $\sigma = Nq^2D/k_B T$, where N is the density of mobile ions, q the elementary charge, k_B the Boltzmann constant and T the temperature [84], one can anticipate that a system with lower ionic conductivity will show slower diffusion-related processes, such as the formation and growth of grains during heat treatment.

In halide perovskites materials and devices, the transport of mobile ions is also related to the well-known phenomenon of I - V hysteresis [85,86,87], which may lead to detrimental effects on reliability, reproducibility, and operational stability in perovskite solar cells [88]. To evaluate the I - V hysteresis in the studied materials, we estimated the power losses that occur in current-voltage cycles measured in up and down regimes, using a slow scan rate (0.1 V s⁻¹) to enhance the effects of slow ionic currents, as employed elsewhere [51,89,90]. Regarding our samples, four measurements were done using different electrodes to get representative results. The cycles are given in Supplementary Note 5. The results are shown in Figure 4c. It is important to mention that factors such as the scan rates, sample thicknesses, and electrode materials and configurations are important for quantitative considerations. More on how the scan rates affect the I - V hysteresis in halide perovskites can be found in the literature [91,92] and in Supplementary Note 6. However, as the same operating conditions were employed in samples of same thicknesses and electrodes, the comparison between the results in the studied samples is assumed to be consistent. That said, there is a clear tendency of the composition-dependent I - V hysteresis to follow a trend similar to the observed for σ_{dc} , as expected. Despite the minor differences in the relative order of EA0.1 and AC0.1 in

σ_{dc} and I - V hysteresis, which may be due to the different experimental configurations, there seems to be a direct correlation between the dipoles of the substituent cation and the hindering of ion transport that can be useful in future developments.

We also employed forward steady-state current-voltage measurements to study electronic charge carriers' transport characteristics. To reduce the effects of ion transport in the measurements, we used a faster scan rate of 0.5 V s^{-1} . Additional details on how the scan rate affects the obtained data are given in Supplementary Note 7. In Figure 4d we show experimental current density ($J = I/A$) versus electric field ($E = V/L$) curves converted from the measured I - V data, from which we note a remarkable reduction in the current density values in the order $\text{MAPbI}_3 > \text{GA0.1} > \text{EA0.1} > \text{AC0.1}$. Also, we note that the profile of the J - E curves appears to be very sensitive to what are the substituting cations. Both observations were pointed out in earlier results in the $\text{GA}_x\text{FA}_y\text{MA}_{1-x-y}\text{PbI}_3$ system [40,90], attributed to the sizes of the cations and the substitution degree. Hence, it is interesting that other factors may play a relevant role in the characteristics of electronic carrier transport. To explore a little further, we note that at low electric fields, the slopes of $\log J$ vs $\log E$ curves are close to 1, indicating the expected ohmic conduction regimes at which $J = \sigma_{ohmic}E$, where σ_{ohmic} is the ohmic conductivity. Using the J - E curves of four measurements in different electrodes, we obtained σ_{ohmic} values for the studied samples, given in Supplementary Note 8. The results are shown in Figure 4e, from which we clearly see that the ohmic conductivity follows the same trend as the current density. Now, to delve into possible electronic characteristics responsible for such, the J - E data had to be modeled with other proper physical models. Similar data in halide perovskites are often modeled using the well-known space charge-limited current (SCLC) approach. However, the expected common features of Mott-Gurney ($J \propto E^2$) and trap-filling ($J \propto E^n, n > 2$) regimes were only identified in the AC0.1 composition. For MAPI and EA0.1, there seems to be a direct change from the ohmic at low E to the Mott-Gurney regime at high E , without an intermediate trap-filling regime typical of the SCLC behavior. To extract the desired electronic carrier parameter, namely, the charge carrier mobility (μ_e), in AC0.1, MAPI, EA0.1, we employed the well-known Mott-Gurney law, given by $J = 9\varepsilon_0\varepsilon'\mu_e E^2/8L$, where ε_0 is the permittivity of free space, ε' the relative dielectric permittivity of the material (Supplementary Note 9), at the high E region where the slope in the $\log J$ vs $\log E$ curves are close to 2. As for For GA0.1, the slope in the $\log J$ vs $\log E$ curves at the high E region are close to 1.5, meaning a $J \propto E^{3/2}$ behavior, typical

of ballistic conduction regimes [93,94]. This type of conduction regime was observed in thick halide perovskite samples [95], including the $\text{GA}_x\text{FA}_y\text{MA}_{1-x-y}\text{PbI}_3$ system [40,90]. Herein, we fitted full J - E curves using a ballistic-like model derived from formal treatments of [95] and [96], given by $J = \varepsilon_0 \varepsilon' \mu_e (4\pi^2 k_B T E / q L^2 + \sqrt{2E_0} E^{3/2})$, where E_0 is the electric field in the transition from the ohmic to the ballistic-like transport. This equation, but in terms of the applied voltage, was recently employed to fit full J - V curves and directly extract μ_e estimations in some $\text{GA}_x\text{FA}_y\text{MA}_{1-x-y}\text{PbI}_3$ compositions [90]. The extracted μ_e values for all present compositions are given in the Supplementary Note 10. The summary of these results are presented in Figure 4f.

It must be stressed that, despite the considerably different J - E profiles that were treated with different models, the changes in behavior between measurements can be related to subtle changes between the relative densities of electronic carriers, mobile ions and traps, sample thicknesses, etc. [97,98,99,100,101]. In this sense, these changes in profile and, consequently, in the physical models used are assumed to be of lesser impact for comparative purposes between the parameters extracted for the studied compositions. For better quantitative assessments, models based on drift-diffusion equations should be used [102], whose complexity level is beyond the present work's purpose. That said, there is a remarkable variation between the estimated μ_e values between the compositions, all within the wide range of values reported in the literature using many techniques [103]. Considering that the same earlier trends hold for μ_e , we conclude that it is the main responsible for the changes in the current-density features. This is somewhat expected given that other important parameters, namely, the density of charge carriers, are in the same order for all compositions (from ~ 2 to $8 \cdot 10^{10} \text{ cm}^{-3}$, also given in Supplementary Note 10). In an intrinsic semiconductor, the density of electronic carriers in thermal equilibrium with the lattice at the dark depends mostly on the band gap energy, which should be very similar in all studied compositions. Even though we did not determine these values, it is known that the A-site cations have only indirect effects on the band gap energy of halide perovskites [104], which are in the range from 1.47 to 1.53 eV in the parent $\text{GA}_x\text{FA}_y\text{MA}_{1-x-y}\text{PbI}_3$ system, leading to comparable electronic carrier densities of about 3 to $7 \cdot 10^{10} \text{ cm}^{-3}$ [90]. To explain the μ_e trend, we first point that substitutionals promote the scattering of charge carriers through lattice distortion and heterogeneity in the mixed-cation compositions, leading to the mobility decrease in the solid solutions compared to MAPbI_3 . The possibility of GA^+ being less effective than EA^+ and AC^+ in

diminishing mobility might be related to the fact that the former is non-polar, while the latter are polar cations. In principle, the cations may enhance the carrier interaction directly through their intrinsic dielectric moment or the polarization of the lattice, reducing their mobility similarly to the dielectric drag effect proposed for halide perovskites [105]. Even though EA⁺ is more polar than AC⁺, we hypothesize that the intensified effect of AC⁺ may be due to its π electrons, leading to electrostatic interactions with charge carriers and potentially promoting drift velocity reduction. Additional theoretical and experimental studies to elucidate the role of these scattering sources would be welcome.

The last characteristic to consider is the stability of the studied materials. It is known that halide perovskites are subject to degradation caused by a series of factors, including humidity, light, oxygen, heat, and applied voltages [106]. To evaluate the relative stability of the materials, we submitted the samples to constant illumination for up to 120 h. The results are shown in Figure 5. In Figure 5a we show the effect of constant illumination from different perspectives. For MAPbI₃, the time-dependent XRD results show that the perovskite peaks, denoted as “pkv”, in the initially phase-pure material progressively become less intense with time under illumination. Meanwhile, the PbI₂ peak increases with time and becomes the main phase after the end of the experiment. Indeed, when the visual aspects of the sample are compared, we observe the clear change from the initial black to the final yellow color, characteristic of the extensive formation of PbI₂. From the chemical reaction perspective, in an oxygen-containing atmosphere, the light-accelerated degradation in MAPbI₃-based perovskites may proceed initially by the process given by $2\text{CH}_3\text{NH}_3\text{PbI}_3 + y\text{O}_2 \xrightarrow{\lambda} 2\text{CH}_3\text{NH}_2 + \text{PbI}_2 + 2\text{I}_2 + \text{PbO}_{(2y-1)} + \text{H}_2\text{O}$, where CH₃NH₃⁺ is the MA⁺ cation [107]. Due to the formation of chemical species in the gas/vapor phase (CH₃NH₂, I₂, and H₂O), an appreciable mass loss occurs, leading to the formation of voids, pores, and an ultimately deteriorated microstructure, as can be seen from the comparison between the initial and final microstructure of MAPbI₃. These aspects, i.e., the time-progressive formation of PbI₂, sample yellowing, and microstructural deterioration, are also observed in the other compositions. In EA0.1 and AC0.1, the phase evolution seems qualitatively similar to MAPbI₃, with the quick disappearance of the perovskite phase and continuous formation of PbI₂, remaining the main final phase. However, for GA0.1, the XRD perovskite peaks remain almost unchanged, indicating little light-accelerated reaction as the formation of PbI₂ is strongly

mitigated. As a consequence, the final aspect of the sample is shown to be much less yellow, and the microstructure remains well-preserved. This result indicates that GA0.1 is much more stable than the other tested compositions.

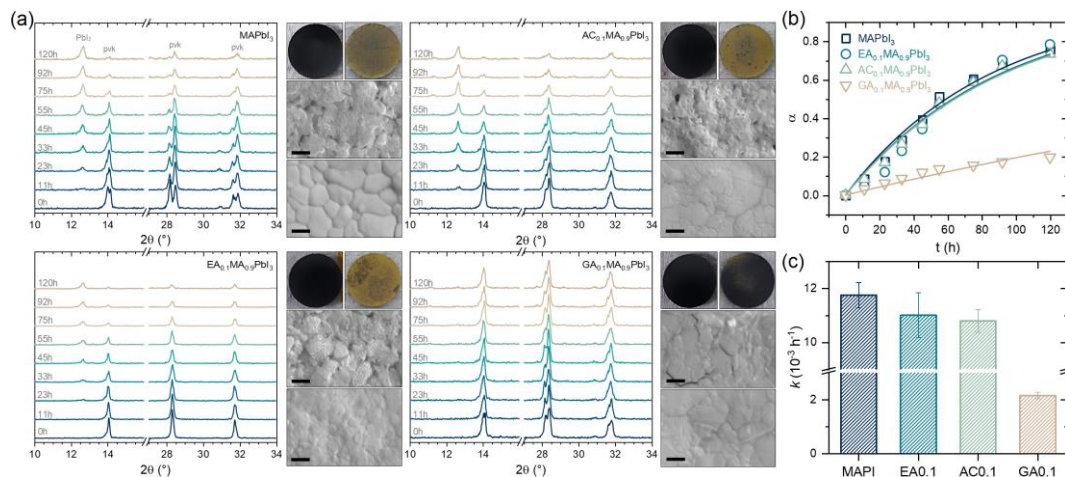


Figure 5 - (a) XRD data of samples submitted to different light-accelerated test times. The “pvk” peaks are of the perovskite phase. Photographs show the samples’ pristine (left) and final (right) visual aspects. Down SEM images are of pristine samples (the same as shown in Figure 1, repeated for clarity), and top images are after the illumination test. Scale bars are 1 μm . (b) Degradation extent as a function of illumination time. Symbols are the experimental data and lines fit the first-order kinetic law equation. (c) Extracted kinetic constant values from the fitted data. Error bars are the fit residuals.

For a quantitative comparison, we modeled the light-accelerated degradation kinetics of the materials using the time-dependent XRD data. To do so, we considered the sum of areas (integrated intensities) of the perovskite peaks proportional to the amount of perovskite phase in a given composition-time condition. Then, we defined the time-dependent degradation extent $\alpha(t)$ of the perovskite phase by $\alpha(t) = 1 - A(t)/A_0$, where A_0 and $A(t)$ is the sum of perovskite peaks at the initial and given time of the light degradation test, respectively. This same procedure was recently applied for temperature-induced degradation experiments [40,41], with the limitations of using the areas well addressed elsewhere [108,109]. The data obtained for each composition are shown in Figure 5b, from which we note the evolution of the degradation extent is essentially equal for MAPbI₃, EA0.1, and AC0.1, and much less intense for GA0.1. Now, to estimate a kinetic constant (k) for the light-accelerated degradation of the materials, the $\alpha(t)$ data were fitted using a first-order kinetic law of the type $\alpha(t) = 1 - \exp(-kt)$, as derived elsewhere [40,41], which is equal to the JMAK equation for an Avrami exponent of 1. The results for the extracted k values are given in Figure 5c, confirming that MAPbI₃,

EA0.1, and AC0.1 presented essentially the same stability against the environmental conditions used in this test, while GA0.1 appear to be less prone to degradation, with a k value more than five times lower than the other compositions. This striking result contrasts with the one found recently, showing that GA-containing compositions may have higher degradation kinetic constants than the MAPbI₃ under high-temperature conditions [40,41]. However, it has to be pointed out that under such conditions, the GA⁺-containing compositions showed a perovskite phase degradation following a second-order kinetic law, with extensive parallel formation of both PbI₂ and GAPbI₃. In the present case, minor GAPbI₃ formation could be identified at ~11.2°, but apparently not extensively enough to modify the kinetic law, here assumed to be of first-order. Noteworthy, the AC0.1 composition does show an appreciable formation of another phase, also identified at ~11.2°, possibly due to the segregation of ACPbI₃, but maybe still not extensively enough to change the kinetic law. Either way, this observation corroborates that secondary non-perovskite APbI₃ phases have been formed in mixed systems where the substituting A-cation has a low solubility limit. Indeed, the AC_xMA_{1-x}PbI₃ system is expected to possess a solubility limit at around $x = 0.2$. This phenomenon seems to be triggered by the elimination of the volatiles in MAPbI₃-based halide perovskites, which in the GA_xFA_yMA_{1-x-y}PbI₃ system, are essentially related only to the MA⁺-derived compounds [41]. Hence, by analogy, we infer that in the studied compositions, the cations EA⁺, GA⁺, and AC⁺ are not volatilized from the materials, and the only eliminations are of MA⁺-related compounds. Due to configurational entropy stabilizations, solid solutions are expected to have lower free energies than pure systems. However, as clearly shown, the entropy of mixing cannot be the only factor since the effects of the cations are severely different. Evidence in current literature regarding hybrid halide perovskites suggests that light-accelerated degradation in the oxygen-containing atmosphere starts through a deprotonation reaction [107]. Since GA⁺ cations have delocalized electron densities, they might be less prone to deprotonation, as expected from the pK_a values of the cations (GA⁺: 13.7, AC⁺: 12.52 [110], EA⁺: 10.87 [111], and MA⁺: 10.66 [112]), there should be fewer protons available to proceed with the reaction. On the other hand, it does not explain why EA⁺ and AC⁺ cations provoke almost no change in the stability of the perovskite. It is an experimental fact that we could not completely dry the atmosphere. Indeed, the relative humidity throughout the experiment was about 50 %, which is quite high when dealing with halide perovskites. Hence, despite the efforts to make an illumination-controlled degradation test, we cannot rule out the

potential role of local water in the degradation of our samples. An irreversible water-induced degradation pathway of MAPbI₃-based perovskites can be represented by the global equation given by $\text{CH}_3\text{NH}_3\text{PbI}_3 \xrightarrow{\text{H}_2\text{O}} \text{CH}_3\text{NH}_2 + \text{HI} + \text{PbI}_2$ [113], which also leaves solid PbI₂ by eliminating volatiles, leading to similar XRD, SEM, and visual aspect changes. Hence, with the existing results, we cannot conclude what the dominant reactions are taking place in the degradation of the tested samples. However, in the case of water-induced processes, one explanation for why EA⁺ and AC⁺ perovskites do not appreciably enhance the stability of the perovskite lies in these cations, possibly conferring a higher hygroscopicity to the samples. As is shown in Supplementary Note 11, the precursor salts ACI and EAI are much more hygroscopic than MAI and GAI. The ACI precursor shows strong deliquescence, becoming a homogeneous aqueous solution in less than one hour, a period on which the EAI precursor was extensively dissolved, while MAI and GAI showed no signs of change. With that in mind, likely, any entropy and acidity-reduction effects that would take place to stabilize the perovskite with EA⁺ and AC⁺ are counterbalanced by the increased hygroscopicity. On the other hand, the incorporation of GA⁺ cations may have all these factors in its favor. Regardless of the reasons, it is clear that GA⁺ cations are more effective than EA⁺ and AC⁺ in increasing the stability against light/humidity-induced degradation.

4. CONCLUSIONS

Using a combination of experimental techniques, we characterized the (micro)structure, electrical behavior, and stability of MAPbI₃-based solid solutions with the same substitution degree of large GA⁺, EA⁺, and AC⁺ cations. Despite having nearly equal sizes, these cations provoke remarkably different changes in the resulting perovskite owing to their combination of other characteristics, e.g., number of N-H bonds, intrinsic dipole moments, acidity, and order of the C-N bonds. The main studied properties, i.e., orthorhombic-to-tetragonal and tetragonal-to-cubic phase transition temperatures, ionic transport, *I-V* hysteresis, *J-E* dependence, electronic conductivity and mobility, and stability against light-accelerated degradation, were evaluated and the differences between the studied compositions interpreted in terms of the characteristics of large cations. The main findings are summarized in Table 3.

Table 3 - Summary of main composition-property relations proposed in this work in GA⁺, AC⁺ or EA⁺-substituted solid solutions compared to the composition with MA⁺ cations only.

Property	Order	Characteristics of large cations due to
T → C temperature	EA ⁺ < AC ⁺ < GA ⁺ < MA ⁺	Lowers with reduced rotational entropy and higher distortion for higher n_{NH}
O → T temperature	GA ⁺ < AC ⁺ < EA ⁺ < MA ⁺	Reasons still unclear, as in [42]
Ionic conductivity	AC ⁺ ≈ EA ⁺ < GA ⁺ < MA ⁺	Lowers with the intrinsic dipole moment due to higher electrostatic repulsion
<i>I-V</i> hysteresis	AC ⁺ ≈ EA ⁺ < GA ⁺ < MA ⁺	Same as the ionic conductivity
Electronic mobility	AC ⁺ < EA ⁺ < GA ⁺ < MA ⁺	Lowers with the intrinsic dipole moment, intensified by double bonds
Stability	GA ⁺ > AC ⁺ ≈ EA ⁺ ≈ MA ⁺	Increases the less acidic and hygroscopic is the cation

Despite the advances, direct correlations with the characteristics of the organic cations were difficult to access in some cases, indicating that the properties of perovskites are a combination of these and other characteristics that were not considered. In any case, our systematization of results, in combination with information from the literature, should be a good starting point for advancing the fundamental understanding of composition-structure-properties relationships in halide perovskites and will enable better rational design in these important materials for optoelectronic and electrochemical applications.

5. SUPPORTING INFORMATION

The Supporting Information file contains precursor and perovskite masses, photo of the setup used for the light-accelerated degradation test, Le Bail fits of XRD data, cross-section SEM images of samples, I-V data obtained with different measurement conditions, frequency-dependent dielectric permittivity, estimated electronic charge carrier parameters, and time-dependent aspect of precursor organic salt powders exposed to ambient air.

6. ACKNOWLEDGEMENTS

This research was supported by the Fundação de Amparo à Pesquisa do Estado de São Paulo (FAPESP Project: 2017/13769-1), the Coordenação de Aperfeiçoamento de Pessoal de Nível Superior (CAPES-PRINT Project: 88881.310513/2018-01), and the Conselho Nacional de Desenvolvimento Científico e Tecnológico (151319/2023-5). The authors thank Mr. Elton José de Souza for supporting the SEM and DSC experiments.

Authors

Fernando Brondani Minussi - Department of Physics and Chemistry, São Paulo State University, 15385-000, Ilha Solteira-SP, Brazil.

Rogério Marcos da Silva Jr. - Department of Electrical Engineering, São Paulo State University, 15385-000, Ilha Solteira-SP, Brazil

João Carlos Silos Moraes - Department of Physics and Chemistry, São Paulo State University, 15385-000, Ilha Solteira-SP, Brazil.

Eudes Borges de Araújo - Department of Physics and Chemistry, São Paulo State University, 15385-000, Ilha Solteira-SP, Brazil.

Author contributions

F. B. Minussi: conceptualization (leading), methodology (leading), validation (leading), formal analysis (leading), investigation (leading), writing - original draft (leading), writing - review and editing (leading), and visualization (leading). R. M. Silva Jr.: conceptualization (support), methodology (support), investigation (support), writing - review and editing (support), and visualization (leading). J. C. S. Moraes: conceptualization (support), methodology (support), validation (support), investigation (support), resources (support), writing - review and editing (support), and funding acquisition (support). E. B. Araújo: conceptualization (support), methodology (support), resources (leading), writing - original draft (support), writing - review and editing (leading), supervision (leading), project administration (leading), and funding acquisition (leading).

Conflicts of interest

There are no conflicts to declare.

7. REFERENCES

- ¹ Q. A. Akkerman and L. Manna, What Defines a Halide Perovskite?, *ACS Energy Lett.*, 2020, **5**, 604–610.
- ² J. Yan, H. Li, M. H. Aldamasy, C. Frasca, A. Abate, K. Zhao and Y. Hu, Advances in the Synthesis of Halide Perovskite Single Crystals for Optoelectronic Applications, *Chem. Mater.*, 2023, **35**, 2683–2712.
- ³ Y. Cho, H. R. Jung and W. Jo, Halide perovskite single crystals: growth, characterization, and stability for optoelectronic applications, *Nanoscale*, 2022, **14**, 9248–9277.
- ⁴ A. Dey, J. Ye, A. De, E. Debroye, S. K. Ha, E. Bladt, A. S. Kshirsagar, Z. Wang, J. Yin, Y. Wang, L. N. Quan, F. Yan, M. Gao, X. Li, J. Shamsi, T. Debnath, M. Cao, M. A. Scheel, S.

Kumar, J. A. Steele, M. Gerhard, L. Chouhan, K. Xu, X. Wu, Y. Li, Y. Zhang, A. Dutta, C. Han, I. Vincon, A. L. Rogach, A. Nag, A. Samanta, B. A. Korgel, C.-J. Shih, D. R. Gamelin, D. H. Son, H. Zeng, H. Zhong, H. Sun, H. V. Demir, I. G. Scheblykin, I. Mora-Seró, J. K. Stolarczyk, J. Z. Zhang, J. Feldmann, J. Hofkens, J. M. Luther, J. Pérez-Prieto, L. Li, L. Manna, M. I. Bodnarchuk, M. V. Kovalenko, M. B. J. Roeffaers, N. Pradhan, O. F. Mohammed, O. M. Bakr, P. Yang, P. Müller-Buschbaum, P. V. Kamat, Q. Bao, Q. Zhang, R. Krahne, R. E. Galian, S. D. Stranks, S. Bals, V. Biju, W. A. Tisdale, Y. Yan, R. L. Z. Hoye and L. Polavarapu, State of the Art and Prospects for Halide Perovskite Nanocrystals, *ACS Nano*, 2021, **15**, 10775–10981.

⁵ W. A. Dunlap-Shohl, Y. Zhou, N. P. Padture and D. B. Mitzi, Synthetic Approaches for Halide Perovskite Thin Films, *Chem. Rev.*, 2019, **119**, 3193–3295.

⁶ A. K. Jena, A. Kulkarni and T. Miyasaka, Halide Perovskite Photovoltaics: Background, Status, and Future Prospects, *Chem. Rev.*, 2019, **119**, 3036–3103.

⁷ F. Temerov, Y. Baghdadi, E. Rattner and S. Eslava, A Review on Halide Perovskite-Based Photocatalysts: Key Factors and Challenges, *ACS Appl. Energy Mater.*, 2022, **5**, 14605–14637.

⁸ H. Guthrey and J. Moseley, A Review and Perspective on Cathodoluminescence Analysis of Halide Perovskites, *Advanced Energy Materials*, 2020, **10**, 1903840.

⁹ K. Lê, N. Heshmati and S. Mathur, Potential and perspectives of halide perovskites in light emitting devices, *Nano Convergence*, 2023, **10**, 47.

¹⁰ Y. Wu, J. Feng, Z. Yang, Y. Liu and S. (Frank) Liu, Halide Perovskite: A Promising Candidate for Next-Generation X-Ray Detectors, *Advanced Science*, 2023, **10**, 2205536.

¹¹ Best Research-Cell Efficiency Chart, <https://www.nrel.gov/pv/cell-efficiency.html>, (accessed 26 May 2024).

¹² B. Li, S. Li, J. Gong, X. Wu, Z. Li, D. Gao, D. Zhao, C. Zhang, Y. Wang and Z. Zhu, Fundamental understanding of stability for halide perovskite photovoltaics: The importance of interfaces, *Chem*, 2024, **10**, 35–47.

¹³ J. Zhuang, J. Wang and F. Yan, Review on Chemical Stability of Lead Halide Perovskite Solar Cells, *Nano-Micro Lett.*, 2023, **15**, 84.

¹⁴ H. Zhu, S. Teale, M. N. Lintangpradipto, S. Mahesh, B. Chen, M. D. McGehee, E. H. Sargent and O. M. Bakr, Long-term operating stability in perovskite photovoltaics, *Nat Rev Mater*, 2023, **8**, 569–586.

¹⁵ N. Ahn and M. Choi, Towards Long-Term Stable Perovskite Solar Cells: Degradation Mechanisms and Stabilization Techniques, *Advanced Science*, 2024, **11**, 2306110.

¹⁶ K. Liu, S. Rafique, S. F. Musolino, Z. Cai, F. Liu, X. Li, Y. Yuan, Q. Bao, Y. Yang, J. Chu, X. Peng, C. Nie, W. Yuan, S. Zhang, J. Wang, Y. Pan, H. Zhang, X. Cai, Z. Shi, C. Li, H. Wang, L. Deng, T. Hu, Y. Wang, Y. Wang, S. Chen, L. Shi, P. Ayala, J. E. Wulff, A. Yu and Y. Zhan, Covalent bonding strategy to enable non-volatile organic cation perovskite for highly stable and efficient solar cells, *Joule*, 2023, **7**, 1033–1050.

¹⁷ Y. Wang, Y. Cheng, C. Yin, J. Zhang, J. You, J. Wang, J. Wang and J. Zhang, Manipulating Crystal Growth and Secondary Phase PbI₂ to Enable Efficient and Stable Perovskite Solar Cells with Natural Additives, *Nano-Micro Lett.*, 2024, **16**, 183.

-
- ¹⁸ A. N. Iqbal, K. W. P. Orr, S. Nagane, J. Ferrer Orri, T. A. S. Doherty, Y. Jung, Y. Chiang, T. A. Selby, Y. Lu, A. J. Mirabelli, A. Baldwin, Z. Y. Ooi, Q. Gu, M. Anaya and S. D. Stranks, Composition Dictates Octahedral Tilt and Photostability in Halide Perovskites, *Advanced Materials*, 2024, 2307508.
- ¹⁹ M. M. Byranvand, C. Otero-Martínez, J. Ye, W. Zuo, L. Manna, M. Saliba, R. L. Z. Hoye and L. Polavarapu, Recent Progress in Mixed A-Site Cation Halide Perovskite Thin-Films and Nanocrystals for Solar Cells and Light-Emitting Diodes, *Advanced Optical Materials*, 2022, **10**, 2200423.
- ²⁰ D. Ghosh, A. R. Smith, A. B. Walker and M. S. Islam, Mixed A-Cation Perovskites for Solar Cells: Atomic-Scale Insights Into Structural Distortion, Hydrogen Bonding, and Electronic Properties, *Chem. Mater.*, 2018, **30**, 5194–5204.
- ²¹ J. Hieulle, D. Son, A. Jamshaid, X. Meng, C. Stecker, R. Ohmann, Z. Liu, L. K. Ono and Y. Qi, Metal Halide Perovskite Surfaces with Mixed A-Site Cations: Atomic Structure and Device Stability, *Adv Funct Materials*, 2023, **33**, 2211097.
- ²² Y. Li, Y. Wang, Z. Xu, B. Peng and X. Li, Key Roles of Interfaces in Inverted Metal-Halide Perovskite Solar Cells, *ACS Nano*, 2024, **18**, 10688–10725.
- ²³ J.-W. Lee, S. Tan, S. I. Seok, Y. Yang and N.-G. Park, Rethinking the A cation in halide perovskites, *Science*, 2022, **375**, eabj1186.
- ²⁴ J. Tian, D. B. Cordes, A. M. Z. Slawin, E. Zysman-Colman and F. D. Morrison, Progressive Polytypism and Bandgap Tuning in Azetidinium Lead Halide Perovskites, *Inorg. Chem.*, 2021, **60**, 12247–12254.
- ²⁵ M. Mączka, M. Ptak, K. Fedoruk, D. Stefańska, A. Gaḡor, J. K. Zaręba and A. Sieradzki, The lattice symmetrization worked, but with a plot twist: effects of methylhydrazinium doping of MAPbI₃ on phase transitions, cation dynamics and photoluminescence, *J. Mater. Chem. C*, 2024, **12**, 1396–1405.
- ²⁶ M. Mączka, M. Ptak, A. Gaḡor, J. K. Zaręba, X. Liang, S. Balčiūnas, O. A. Semenikhin, O. I. Kucheriv, I. A. Gural'skiy, S. Shova, A. Walsh, J. Banys and M. Šimėnas, Phase Transitions, Dielectric Response, and Nonlinear Optical Properties of Aziridinium Lead Halide Perovskites, *Chem. Mater.*, 2023, **35**, 9725–9738.
- ²⁷ Q. Wang, F. Lin, C.-C. Chueh, T. Zhao, M. Eslamian and A. K.-Y. Jen, Enhancing efficiency of perovskite solar cells by reducing defects through imidazolium cation incorporation, *Materials Today Energy*, 2018, **7**, 161–168.
- ²⁸ G. Kieslich, S. Sun and A. K. Cheetham, Solid-state principles applied to organic–inorganic perovskites: new tricks for an old dog, *Chem. Sci.*, 2014, **5**, 4712–4715.
- ²⁹ G. Kieslich, S. Sun and A. K. Cheetham, An extended Tolerance Factor approach for organic–inorganic perovskites, *Chem. Sci.*, 2015, **6**, 3430–3433.
- ³⁰ C. J. Bartel, C. Sutton, B. R. Goldsmith, R. Ouyang, C. B. Musgrave, L. M. Ghiringhelli and M. Scheffler, New tolerance factor to predict the stability of perovskite oxides and halides, *Sci. Adv.*, 2019, **5**, eaav0693.
- ³¹ H. B. Lee, N. Kumar, B. Tyagi, S. He, R. Sahani and J.-W. Kang, Bulky organic cations engineered lead-halide perovskites: a review on dimensionality and optoelectronic applications, *Materials Today Energy*, 2021, **21**, 100759.

-
- ³² H. Park, S. Kumar, S. Chawla and F. El-Mellouhi, Design Principles of Large Cation Incorporation in Halide Perovskites, *Molecules*, 2021, **26**, 6184.
- ³³ H. Park, A. Ali, R. Mall, H. Bensmail, S. Sanvito and F. El-Mellouhi, Data-driven enhancement of cubic phase stability in mixed-cation perovskites, *Mach. Learn.: Sci. Technol.*, 2021, **2**, 025030.
- ³⁴ F. Ünlü, E. Jung, J. Haddad, A. Kulkarni, S. Öz, H. Choi, T. Fischer, S. Chakraborty, T. Kirchartz and S. Mathur, Understanding the interplay of stability and efficiency in A-site engineered lead halide perovskites, *APL Materials*, 2020, **8**, 070901.
- ³⁵ C. Wu, D. Guo, P. Li, S. Wang, A. Liu and F. Wu, A study on the effects of mixed organic cations on the structure and properties in lead halide perovskites, *Phys. Chem. Chem. Phys.*, 2020, **22**, 3105–3111.
- ³⁶ S. Jin, Can We Find the Perfect A-Cations for Halide Perovskites?, *ACS Energy Lett.*, 2021, **6**, 3386–3389.
- ³⁷ D. W. Ferdani, S. R. Pering, D. Ghosh, P. Kubiak, A. B. Walker, S. E. Lewis, A. L. Johnson, P. J. Baker, M. S. Islam and P. J. Cameron, Partial cation substitution reduces iodide ion transport in lead iodide perovskite solar cells, *Energy Environ. Sci.*, 2019, **12**, 2264–2272.
- ³⁸ F. B. Minussi, R. M. da Silva and E. B. Araújo, Does it mix? Insights and attempts to predict the formability of single phase mixed A-cation lead iodide perovskites, *Inorg. Chem. Front.*, 2023, **10**, 6129–6133.
- ³⁹ P. Singh, R. Mukherjee and S. Avasthi, Acetamidinium-Substituted Methylammonium Lead Iodide Perovskite Solar Cells with Higher Open-Circuit Voltage and Improved Intrinsic Stability, *ACS Appl. Mater. Interfaces*, 2020, **12**, 13982–13987.
- ⁴⁰ F. B. Minussi, R. M. Da Silva and E. B. Araújo, Differing Effects of Mixed A-Site Composition on the Properties of Hybrid Lead Iodide Perovskites, *J. Phys. Chem. C*, 2023, **127**, 8814–8824.
- ⁴¹ F. B. Minussi, R. M. Silva, J. F. Carvalho and E. B. Araújo, Thermal degradation in methylammonium–formamidinium–guanidinium lead iodide perovskites, *J. Mater. Chem. C*, 2024, **12**, 5138–5149.
- ⁴² F. B. Minussi, R. M. Silva and E. B. Araújo, Composition-Property Relations for $\text{GA}_x\text{FA}_y\text{MA}_{1-x-y}\text{PbI}_3$ Perovskites, *Small*, 2024, **20**, 2305054.
- ⁴³ M. Simenas, A. Gagor, J. Banys and M. Maczka, Phase Transitions and Dynamics in Mixed Three- and Low-Dimensional Lead Halide Perovskites, *Chem. Rev.*, 2024, **124**, 2281–2326.
- ⁴⁴ W. Geng, Q. Hu, C. Tong, Z. Tang and L. Liu, The Influence of Dipole Moments Induced by Organic Molecules and Domain Structures on the Properties of $\text{CH}_3\text{NH}_3\text{PbI}_3$ Perovskite, *Advcd Theory and Sims*, 2019, **2**, 1900041.
- ⁴⁵ S. Maheshwari, S. Patwardhan, G. C. Schatz, N. Renaud and F. C. Grozema, The effect of the magnitude and direction of the dipoles of organic cations on the electronic structure of hybrid halide perovskites, *Phys. Chem. Chem. Phys.*, 2019, **21**, 16564–16572.
- ⁴⁶ S. Maheshwari, M. B. Fridriksson, S. Seal, J. Meyer and F. C. Grozema, The Relation between Rotational Dynamics of the Organic Cation and Phase Transitions in Hybrid Halide Perovskites, *J. Phys. Chem. C*, 2019, **123**, 14652–14661.
- ⁴⁷ M. Pazoki, M. J. Wolf, T. Edvinsson and J. Kullgren, Vacancy dipole interactions and the

correlation with monovalent cation dependent ion movement in lead halide perovskite solar cell materials, *Nano Energy*, 2017, **38**, 537–543.

⁴⁸ M. Šimėnas, S. Balčiūnas, A. Gągor, A. Pieniżek, K. Tolborg, M. Kinka, V. Klimavicius, Š. Svirskas, V. Kalendra, M. Ptak, D. Szewczyk, A. P. Herman, R. Kudrawiec, A. Sieradzki, R. Grigalaitis, A. Walsh, M. Mączka and J. Banys, Mixology of MA_{1-x}EA_xPbI₃ Hybrid Perovskites: Phase Transitions, Cation Dynamics, and Photoluminescence, *Chem. Mater.*, 2022, **34**, 10104–10112.

⁴⁹ J. Gebhardt and A. M. Rappe, Mix and Match: Organic and Inorganic Ions in the Perovskite Lattice, *Advanced Materials*, 2019, **31**, 1802697.

⁵⁰ J. H. Jensen and J. C. Kromann, The Molecule Calculator: A Web Application for Fast Quantum Mechanics-Based Estimation of Molecular Properties, *J. Chem. Educ.*, 2013, **90**, 1093–1095.

⁵¹ F. B. Minussi, E. M. Bertolotti, S. P. Reis, J. F. Carvalho and E. B. Araújo, Guanidinium substitution-dependent phase transitions, ionic conductivity, and dielectric properties of MAPbI₃, *Chem. Commun.*, 2022, **58**, 2212–2215.

⁵² B. Huang, Z. Liu, C. Wu, Y. Zhang, J. Zhao, X. Wang and J. Li, Polar or nonpolar? That is not the question for perovskite solar cells, *National Science Review*, 2021, **8**, nwab094.

⁵³ S. Qin, S. Yi, Y. Xu, Z. Mi, J. Zhao, X. Tian, H. Guo, Y. Jiao, G. Zhang and J. Lu, Ferroic alternation in methylammonium lead triiodide perovskite, *EcoMat*, 2021, **3**, e12131.

⁵⁴ A. Poglitsch and D. Weber, Dynamic disorder in methylammoniumtrihalogenoplumbates (II) observed by millimeter-wave spectroscopy, *The Journal of Chemical Physics*, 1987, **87**, 6373–6378.

⁵⁵ T. Baikie, Y. Fang, J. M. Kadro, M. Schreyer, F. Wei, S. G. Mhaisalkar, M. Graetzel and T. J. White, Synthesis and crystal chemistry of the hybrid perovskite (CH₃NH₃)PbI₃ for solid-state sensitised solar cell applications, *J. Mater. Chem. A*, 2013, **1**, 5628–5641.

⁵⁶ T. J. Jacobsson, L. J. Schwan, M. Ottosson, A. Hagfeldt and T. Edvinsson, Determination of Thermal Expansion Coefficients and Locating the Temperature-Induced Phase Transition in Methylammonium Lead Perovskites Using X-ray Diffraction, *Inorg. Chem.*, 2015, **54**, 10678–10685.

⁵⁷ T. Chen, B. J. Foley, C. Park, C. M. Brown, L. W. Harriger, J. Lee, J. Ruff, M. Yoon, J. J. Choi and S.-H. Lee, Entropy-driven structural transition and kinetic trapping in formamidinium lead iodide perovskite, *Sci. Adv.*, 2016, **2**, e1601650.

⁵⁸ C. Yi, J. Luo, S. Meloni, A. Boziki, N. Ashari-Astani, C. Grätzel, S. M. Zakeeruddin, U. Röthlisberger and M. Grätzel, Entropic stabilization of mixed A-cation ABX₃ metal halide perovskites for high performance perovskite solar cells, *Energy Environ. Sci.*, 2016, **9**, 656–662.

⁵⁹ A. Bonadio, C. A. Escanhoela, F. P. Sabino, G. Sombrio, V. G. de Paula, F. F. Ferreira, A. Janotti, G. M. Dalpian and J. A. Souza, Entropy-driven stabilization of the cubic phase of MAPbI₃ at room temperature, *J. Mater. Chem. A*, 2021, **9**, 1089–1099.

⁶⁰ S. Liu, R. Guo and F. Xie, The effects of organic cation rotation in hybrid Organic-Inorganic Perovskites: A critical review, *Materials & Design*, 2022, **221**, 110951.

⁶¹ E. Bi, Z. Song, C. Li, Z. Wu and Y. Yan, Mitigating ion migration in perovskite solar cells, *Trends in Chemistry*, 2021, **3**, 575–588.

-
- ⁶² X. Yan, W. Fan, F. Cheng, H. Sun, C. Xu, L. Wang, Z. Kang and Y. Zhang, Ion migration in hybrid perovskites: Classification, identification, and manipulation, *Nano Today*, 2022, **44**, 101503.
- ⁶³ J.-W. Lee, S.-G. Kim, J.-M. Yang, Y. Yang and N.-G. Park, Verification and mitigation of ion migration in perovskite solar cells, *APL Materials*, 2019, **7**, 041111.
- ⁶⁴ F. B. Minussi, L. A. Silva and E. B. Araújo, Structure, optoelectronic properties and thermal stability of the triple organic cation $\text{GA}_x\text{FA}_x\text{MA}_{1-2x}\text{PbI}_3$ system prepared by mechanochemical synthesis, *Phys. Chem. Chem. Phys.*, 2022, **24**, 4715–4728.
- ⁶⁵ T. Glaser, C. Müller, M. Sendner, C. Krekeler, O. E. Semonin, T. D. Hull, O. Yaffe, J. S. Owen, W. Kowalsky, A. Pucci and R. Lovrinčić, Infrared Spectroscopic Study of Vibrational Modes in Methylammonium Lead Halide Perovskites, *J. Phys. Chem. Lett.*, 2015, **6**, 2913–2918.
- ⁶⁶ D. L. Pavia, G. M. Lampman, G. S. Kriz and J. R. Vyvyan, *Introduction to spectroscopy*, Cengage Learning, Stamford, CT, Fifth edition., 2015.
- ⁶⁷ F. B. Minussi, S. P. Reis and E. B. Araújo, Effects of frequency, temperature, and dc bias electric field on the dielectric properties of methylammonium lead iodide from the perspective of a relaxor-like ferroelectric, *Acta Materialia*, 2021, **219**, 117235.
- ⁶⁸ I. Anusca, S. Balčiūnas, P. Gemeiner, Š. Svirskas, M. Sanlialp, G. Lackner, C. Fettkenhauer, J. Belovickis, V. Samulionis, M. Ivanov, B. Dkhil, J. Banys, V. V. Shvartsman and D. C. Lupascu, Dielectric Response: Answer to Many Questions in the Methylammonium Lead Halide Solar Cell Absorbers, *Advanced Energy Materials*, 2017, **7**, 1700600.
- ⁶⁹ P. S. Whitfield, N. Herron, W. E. Guise, K. Page, Y. Q. Cheng, I. Milas and M. K. Crawford, Structures, Phase Transitions and Tricritical Behavior of the Hybrid Perovskite Methyl Ammonium Lead Iodide, *Sci Rep*, 2016, **6**, 35685.
- ⁷⁰ M. T. Weller, O. J. Weber, P. F. Henry, A. M. Di Pumpo and T. C. Hansen, Complete structure and cation orientation in the perovskite photovoltaic methylammonium lead iodide between 100 and 352 K, *Chem. Commun.*, 2015, **51**, 4180–4183.
- ⁷¹ J. Liu, J. Du, P. B. Wyatt, D. A. Keen, A. E. Phillips and M. T. Dove, Orientational order/disorder and network flexibility in deuterated methylammonium lead iodide perovskite by neutron total scattering, *J. Mater. Chem. A*, 2024, **12**, 2771–2785.
- ⁷² Y.-F. Chen, Y.-T. Tsai, D. M. Bassani and L. Hirsch, Experimental evidence of the anti-parallel arrangement of methylammonium ions in perovskites, *Applied Physics Letters*, 2016, **109**, 213504.
- ⁷³ S. Govinda, B. P. Kore, M. Bokdam, P. Mahale, A. Kumar, S. Pal, B. Bhattacharyya, J. Lahnsteiner, G. Kresse, C. Franchini, A. Pandey and D. D. Sarma, Behavior of Methylammonium Dipoles in MAPbX_3 ($X = \text{Br}$ and I), *J. Phys. Chem. Lett.*, 2017, **8**, 4113–4121.
- ⁷⁴ A. Mohanty, D. Swain, S. Govinda, T. N. G. Row and D. D. Sarma, Phase Diagram and Dielectric Properties of $\text{MA}_{1-x}\text{FA}_x\text{PbI}_3$, *ACS Energy Lett.*, 2019, **4**, 2045–2051.
- ⁷⁵ A. Francisco-López, B. Charles, M. I. Alonso, M. Garriga, M. Campoy-Quiles, M. T. Weller and A. R. Goñi, Phase Diagram of Methylammonium/Formamidinium Lead Iodide Perovskite Solid Solutions from Temperature-Dependent Photoluminescence and Raman Spectroscopies, *J.*

Phys. Chem. C, 2020, **124**, 3448–3458.

⁷⁶ A. G. Kontos, G. K. Manolis, A. Kaltzoglou, D. Palles, E. I. Kamitsos, M. G. Kanatzidis and P. Falaras, Halogen–NH₂⁺ Interaction, Temperature-Induced Phase Transition, and Ordering in (NH₂CHNH₂)PbX₃ (X = Cl, Br, I) Hybrid Perovskites, *J. Phys. Chem. C*, 2020, **124**, 8479–8487.

⁷⁷ K. S. Cole and R. H. Cole, Dispersion and Absorption in Dielectrics I. Alternating Current Characteristics, *The Journal of Chemical Physics*, 1941, **9**, 341–351.

⁷⁸ A. Bou, A. Pockett, H. Cruanyes, D. Raptis, T. Watson, M. J. Carnie and J. Bisquert, Limited information of impedance spectroscopy about electronic diffusion transport: The case of perovskite solar cells, *APL Materials*, 2022, **10**, 051104.

⁷⁹ M. H. Futscher and C. Deibel, Defect Spectroscopy in Halide Perovskites Is Dominated by Ionic Rather than Electronic Defects, *ACS Energy Lett.*, 2022, **7**, 140–144.

⁸⁰ D. Moia and J. Maier, Ion Transport, Defect Chemistry, and the Device Physics of Hybrid Perovskite Solar Cells, *ACS Energy Lett.*, 2021, **6**, 1566–1576.

⁸¹ T. Zhang, C. Hu and S. Yang, Ion Migration: A “Double-Edged Sword” for Halide-Perovskite-Based Electronic Devices, *Small Methods*, 2020, **4**, 1900552.

⁸² C. Eames, J. M. Frost, P. R. F. Barnes, B. C. O’Regan, A. Walsh and M. S. Islam, Ionic transport in hybrid lead iodide perovskite solar cells, *Nat Commun*, 2015, **6**, 7497.

⁸³ T. Yang, G. Gregori, N. Pellet, M. Grätzel and J. Maier, The Significance of Ion Conduction in a Hybrid Organic–Inorganic Lead-Iodide-Based Perovskite Photosensitizer, *Angew Chem Int Ed*, 2015, **54**, 7905–7910.

⁸⁴ C. B. Carter and M. G. Norton, *Ceramic materials: science and engineering*, Springer, New York, Second edition., 2013.

⁸⁵ G. Richardson, S. E. J. O’Kane, R. G. Niemann, T. A. Peltola, J. M. Foster, P. J. Cameron and A. B. Walker, Can slow-moving ions explain hysteresis in the current–voltage curves of perovskite solar cells?, *Energy Environ. Sci.*, 2016, **9**, 1476–1485.

⁸⁶ S. N. Habisreutinger, N. K. Noel and H. J. Snaith, Hysteresis Index: A Figure without Merit for Quantifying Hysteresis in Perovskite Solar Cells, *ACS Energy Lett.*, 2018, **3**, 2472–2476.

⁸⁷ J. Bisquert, Electrical Charge Coupling Dominates the Hysteresis Effect of Halide Perovskite Devices, *J. Phys. Chem. Lett.*, 2023, **14**, 1014–1021.

⁸⁸ F. Wu, R. Pathak and Q. Qiao, Origin and alleviation of J-V hysteresis in perovskite solar cells: A short review, *Catalysis Today*, 2021, **374**, 86–101.

⁸⁹ F. B. Minussi, E. M. Bertolotti, J. A. Eiras and E. B. Araújo, Intrinsic aging in mixed-cation lead halide perovskites, *Sustainable Energy Fuels*, 2022, **6**, 4925–4937.

⁹⁰ F. B. Minussi, R. M. Silva and E. B. Araújo, Interplay between cation composition and charge transport characteristics in GAxFAyMA1-x-y PbI3 halide perovskites, *Applied Physics Letters*, 2024, **124**, 153901.

⁹¹ G. Garcia-Belmonte and J. Bisquert, Distinction between Capacitive and Noncapacitive Hysteretic Currents in Operation and Degradation of Perovskite Solar Cells, *ACS Energy Lett.*, 2016, **1**, 683–688.

-
- ⁹² S. Tammireddy, M. N. Lintangpradipto, O. Telschow, M. H. Futscher, B. Ehrler, O. M. Bakr, Y. Vaynzof and C. Deibel, Hysteresis and Its Correlation to Ionic Defects in Perovskite Solar Cells, *J. Phys. Chem. Lett.*, 2024, **15**, 1363–1372.
- ⁹³ C. D. Child, Discharge From Hot CaO, *Phys. Rev. (Series I)*, 1911, **32**, 492–511.
- ⁹⁴ I. Langmuir, The Effect of Space Charge and Residual Gases on Thermionic Currents in High Vacuum, *Phys. Rev.*, 1913, **2**, 450–486.
- ⁹⁵ O. Almora, D. Miravet, M. García-Batlle and G. Garcia-Belmonte, Ballistic-like space-charge-limited currents in halide perovskites at room temperature, *Applied Physics Letters*, 2021, **119**, 242107.
- ⁹⁶ J. A. Röhr and R. C. I. MacKenzie, Analytical description of mixed ohmic and space-charge-limited conduction in single-carrier devices, *Journal of Applied Physics*, 2020, **128**, 165701.
- ⁹⁷ E. A. Duijnste, J. M. Ball, V. M. Le Corre, L. J. A. Koster, H. J. Snaith and J. Lim, Toward Understanding Space-Charge Limited Current Measurements on Metal Halide Perovskites, *ACS Energy Lett.*, 2020, **5**, 376–384.
- ⁹⁸ V. M. Le Corre, E. A. Duijnste, O. El Tambouli, J. M. Ball, H. J. Snaith, J. Lim and L. J. A. Koster, Revealing Charge Carrier Mobility and Defect Densities in Metal Halide Perovskites via Space-Charge-Limited Current Measurements, *ACS Energy Lett.*, 2021, **6**, 1087–1094.
- ⁹⁹ M. Sajedi Alvar, P. W. M. Blom and G.-J. A. H. Wetzelaer, Space-charge-limited electron and hole currents in hybrid organic-inorganic perovskites, *Nat Commun*, 2020, **11**, 4023.
- ¹⁰⁰ J. A. Röhr, D. Moia, S. A. Haque, T. Kirchartz and J. Nelson, Exploring the validity and limitations of the Mott–Gurney law for charge-carrier mobility determination of semiconducting thin-films, *J. Phys.: Condens. Matter*, 2018, **30**, 105901.
- ¹⁰¹ A. Zhao, V. M. Le Corre and J. A. Röhr, On the importance of varying device thickness and temperature on the outcome of space-charge-limited current measurements, *Front. Electron. Mater.*, DOI:10.3389/femat.2024.1396521.
- ¹⁰² K. Sivula, Improving Charge Carrier Mobility Estimations When Using Space-Charge-Limited Current Measurements, *ACS Energy Lett.*, 2022, **7**, 2102–2104.
- ¹⁰³ L. M. Herz, Charge-Carrier Mobilities in Metal Halide Perovskites: Fundamental Mechanisms and Limits, *ACS Energy Lett.*, 2017, **2**, 1539–1548.
- ¹⁰⁴ A. Walsh, Principles of Chemical Bonding and Band Gap Engineering in Hybrid Organic–Inorganic Halide Perovskites, *J. Phys. Chem. C*, 2015, **119**, 5755–5760.
- ¹⁰⁵ M. Bonn, K. Miyata, E. Hendry and X.-Y. Zhu, Role of Dielectric Drag in Polaron Mobility in Lead Halide Perovskites, *ACS Energy Lett.*, 2017, **2**, 2555–2562.
- ¹⁰⁶ A. Senocrate, G. Y. Kim, M. Grätzel and J. Maier, Thermochemical Stability of Hybrid Halide Perovskites, *ACS Energy Lett.*, 2019, **4**, 2859–2870.
- ¹⁰⁷ S. Ruan, M.-A. Surmiak, Y. Ruan, D. P. McMeekin, H. Ebendorff-Heidepriem, Y.-B. Cheng, J. Lu and C. R. McNeill, Light induced degradation in mixed-halide perovskites, *J. Mater. Chem. C*, 2019, **7**, 9326–9334.
- ¹⁰⁸ T. Burwig and P. Pistor, Reaction kinetics of the thermal decomposition of MAPbI₃ thin films, *Phys. Rev. Mater.*, 2021, **5**, 065405.

-
- ¹⁰⁹ T. Burwig, K. Heinze and P. Pistor, Thermal decomposition kinetics of FAPbI₃ thin films, *Phys. Rev. Mater.*, 2022, **6**, 065404.
- ¹¹⁰ R. Williams, Bordwell pKa Table, pKa Values in Water Compilation, <https://organicchemistrydata.org/hansreich/resources/pka/>, (accessed 26 May 2024).
- ¹¹¹ PubChem, Hazardous Substances Data Bank (HSDB), <https://pubchem.ncbi.nlm.nih.gov/source/hsdb/803>, (accessed 26 May 2024).
- ¹¹² PubChem, Hazardous Substances Data Bank (HSDB), <https://pubchem.ncbi.nlm.nih.gov/source/hsdb/810>, (accessed 26 May 2024).
- ¹¹³ P. Toloueinia, H. Khassaf, A. Shirazi Amin, Z. M. Tobin, S. P. Alpay and S. L. Suib, Moisture-Induced Structural Degradation in Methylammonium Lead Iodide Perovskite Thin Films, *ACS Appl. Energy Mater.*, 2020, **3**, 8240–8248.

SUPPORTING INFORMATION

Organic cations in halide perovskite solid solutions: exploring beyond size effects

F. B. Minussi^{1*}, R. M. Silva Jr.², J. C. S. Moraes¹, E. B. Araújo¹

¹ Department of Physics and Chemistry, São Paulo State University, 15385-007, Ilha Solteira, SP - Brazil

² Department of Electrical Engineering, São Paulo State University, 15385-007, Ilha Solteira, SP - Brazil

CONTENTS

Supplementary Note 1: Precursor and perovskite masses	1
Supplementary Note 2: Setup for the light-accelerated degradation test	2
Supplementary Note 3: Le Bail fits of XRD data	3
Supplementary Note 4: Thickness of samples	4
Supplementary Note 5: Measurements for <i>I-V</i> hysteresis	5
Supplementary Note 6: Dependence of the <i>I-V</i> hysteresis on scan rate	6
Supplementary Note 7: Dependence of the <i>I-V</i> forward curves on scan rate	7
Supplementary Note 8: Forward <i>I-V</i> measurements	8
Supplementary Note 9: Frequency-dependent dielectric permittivity	9
Supplementary Note 10: Electronic carrier parameters	10
Supplementary Note 11: Changes in precursor organic salts exposed to ambient air	11

* corresponding author: fbminussi@gmail.com

Supplementary Note 1: Precursor and perovskite masses

Table S1 - Weighted reaction precursors and resulting perovskite (HP) masses. Yield is the ratio between the HP obtained and expected (sum of precursors) masses.

Composition	PbI ₂ (g)	MAI (g)	GAI (g)	EAI (g)	ACI (g)	HP (g)	Yield (%)
MAPI	0.901 ₉	0.310 ₆	0	0	0	1.085 ₀	89.5
GA0.1	0.897 ₁	0.278 ₅	0.036 ₀	0	0	1.118 ₇	92.3
EA0.1	0.899 ₃	0.279 ₁	0	0.034 ₁	0	1.109 ₅	91.5
AC0.1	0.898 ₅	0.278 ₃	0	0	0.036 ₀	1.088 ₀	89.7

Supplementary Note 2: Setup for the light-accelerated degradation test



Figure S1 - Home-made setup used for the light-accelerated degradation test. The samples were distributed uniformly in the Petri dish, which was positioned in the center of the rotating (6 Hz clockwise) platform and submitted to direct and mirror-reflected illumination from the LED lamp. The lamp specifications are a power of 6 W, luminous flux of 560 lm, and color cold white (6500 K). The box (30 x 20 x 15 cm) remained closed and sealed with masking tape during the test. Inside humidity was kept as low as possible by drying silica beads. Temperature and relative humidity were constantly monitored.

Supplementary Note 3: Le Bail fits of XRD data

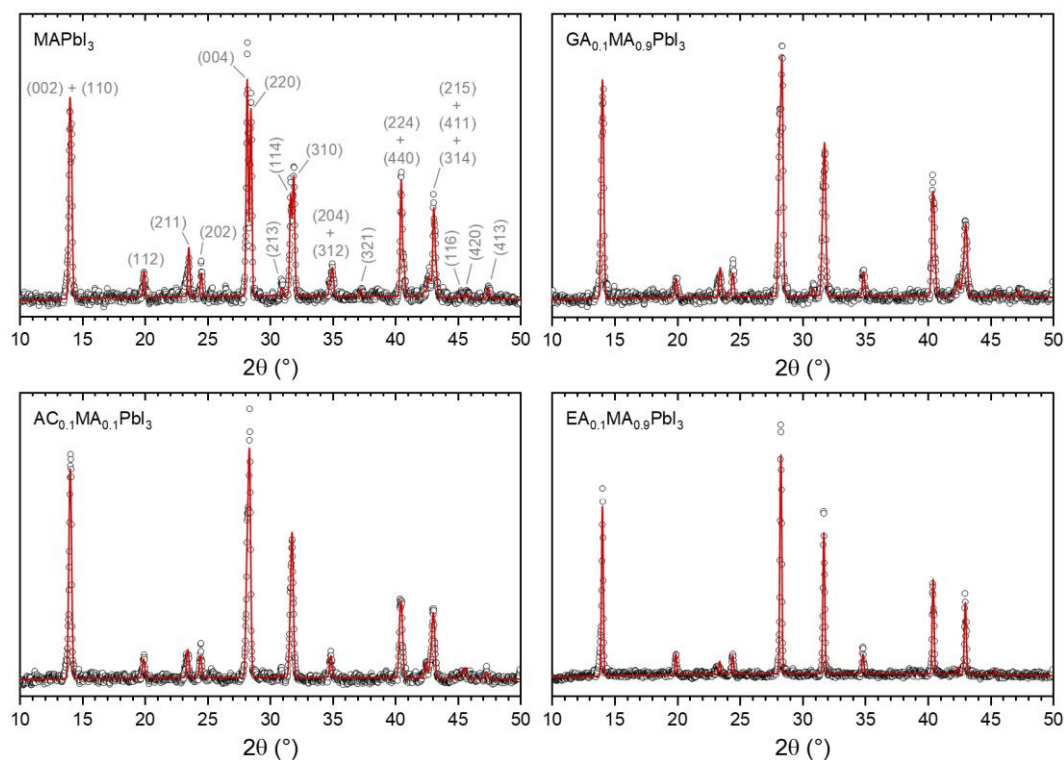


Figure S2 - Experimental data (black dots) and Le Bail fits (red lines) of studied compositions. Fits were calculated using the WinPLOTR package as implemented in the Fullprof software (version of April 2024) considering the $I4cm$ (tetragonal) space groups.

Table S2 - Original lattice parameters obtained through the Le Bail fit.

Composition	a (Å)	c (Å)	χ^2
MAPbI ₃	8.8599 ± 0.0005	12.6600 ± 0.0007	1.75
GA _{0.1} MA _{0.9} PbI ₃	8.8879 ± 0.0005	12.6603 ± 0.0011	1.47
AC _{0.1} MA _{0.9} PbI ₃	8.8905 ± 0.0005	12.6594 ± 0.0014	1.35
EA _{0.1} MA _{0.9} PbI ₃	8.9067 ± 0.0006	12.6184 ± 0.0011	1.63

Supplementary Note 4: Thickness of samples

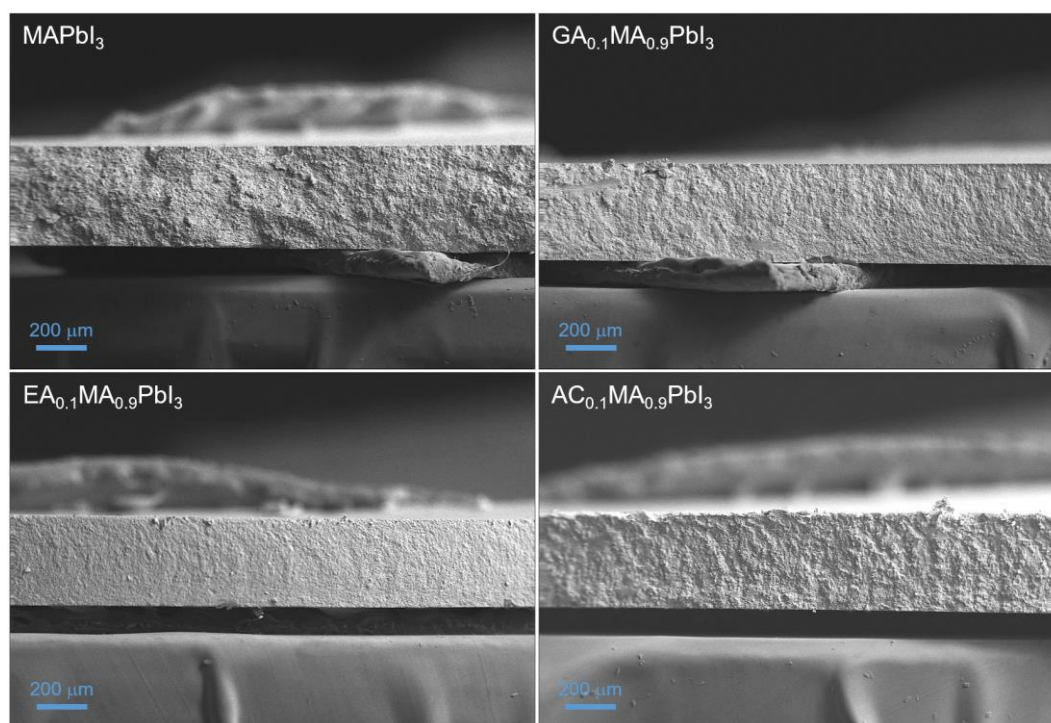


Figure S3 - Cross-section SEM images of the samples used in the electrical characterizations.

Supplementary Note 5: Measurements for I - V hysteresis

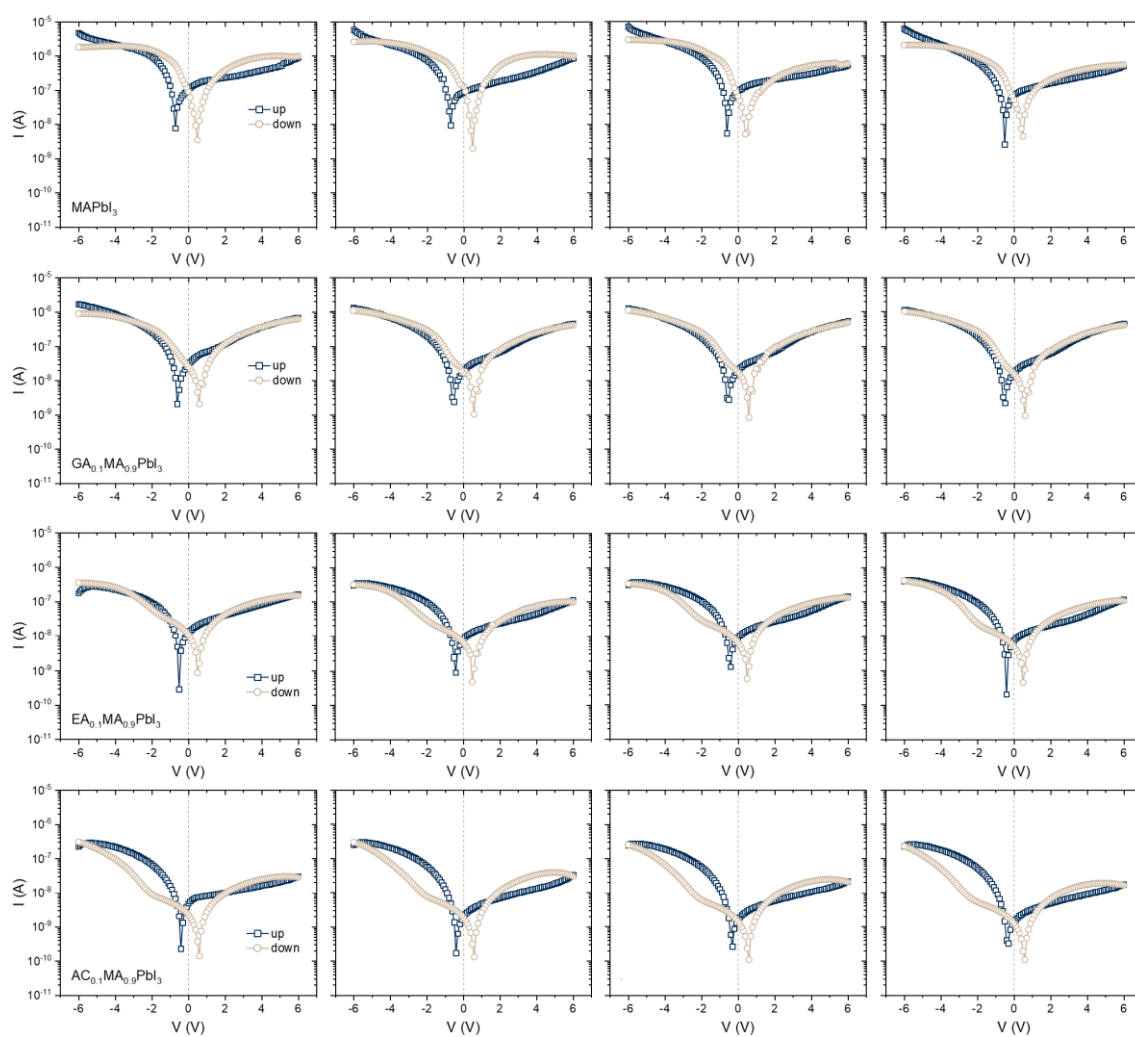


Figure S4 - Four measurements of up and down cycles with a scan rate of 0.1 V s^{-1} used to evaluate the I - V hysteresis.

Supplementary Note 6: Dependence of the I - V hysteresis on scan rate

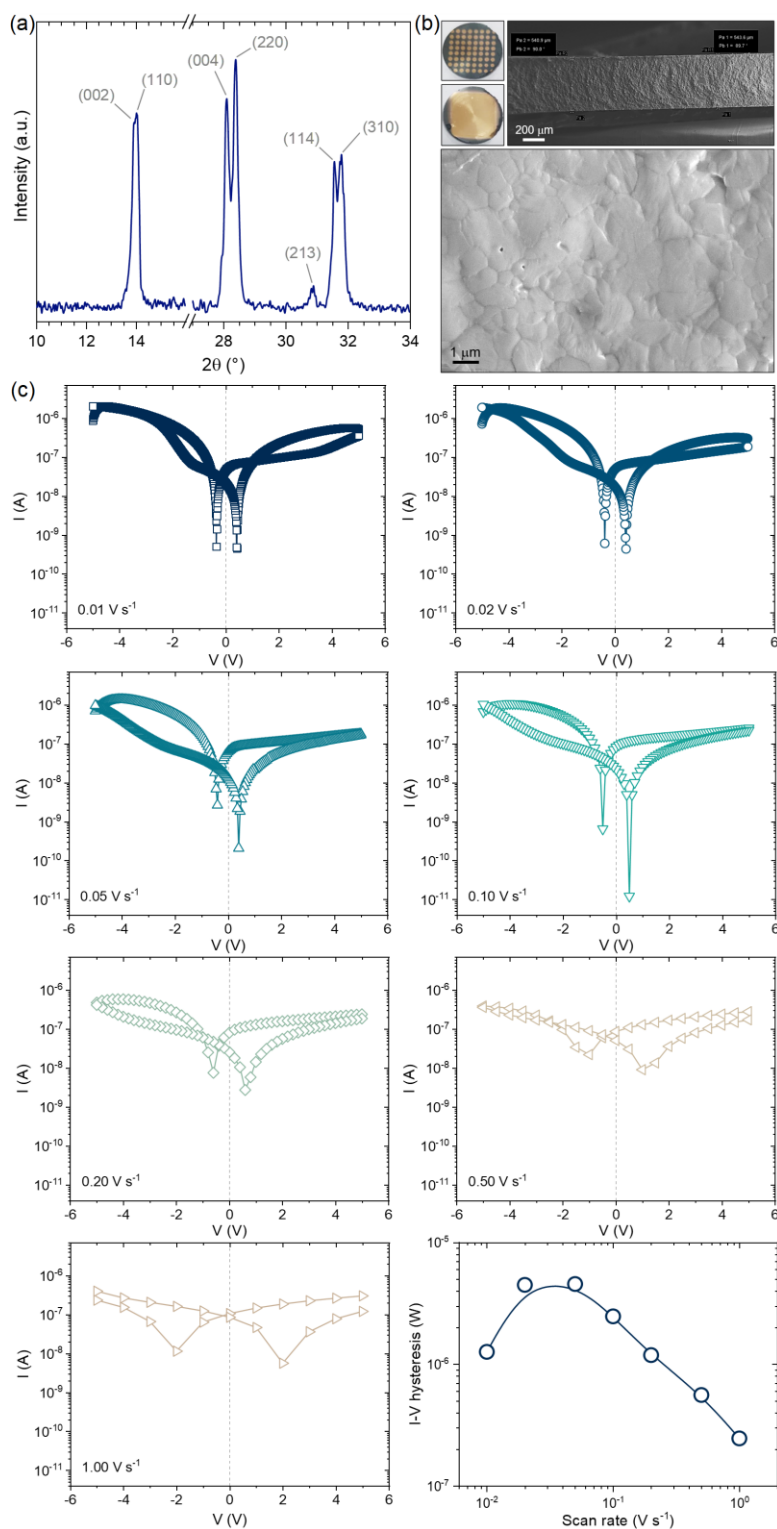


Figure S5 - (a) XRD of another MAPbI_3 sample synthesized to evaluate the effect of the scan rate on the I - V hysteresis. (b) Photograph of the sample with deposited gold electrodes and SEM images of its surface and cross-section. (c) Up and down cycles were measured at different scan rates from 0.01 to 1.00 V s^{-1} and the I - V hysteresis values as a function of the scan rates. The measurements were performed at the same electrode with intervals of more 40 minutes between cycles, starting from higher to lower scan rates.

Supplementary Note 7: Dependence of the I - V forward curves on scan rate

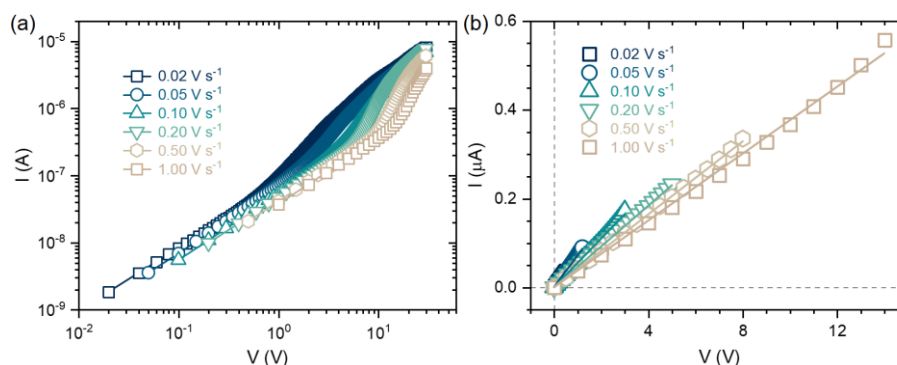


Figure S6 - (a) I - V curves measured with different scan rates. (b) Detail of the low voltage region where the conduction follows an ohmic behavior. The ohmic conductivity is proportional to the slope of lines, i.e., the apparent conductivity increases the lower the scan rate. On the other hand, the deviation from the ohmic regime occurs at lower voltages. All measurements were performed at the sample shown previously and at the same electrode (but different from the one used to collect the data of I - V cycles), with intervals of more than 40 minutes between cycles, starting from higher to lower scan rates.

Supplementary Note 8: Forward I - V measurements

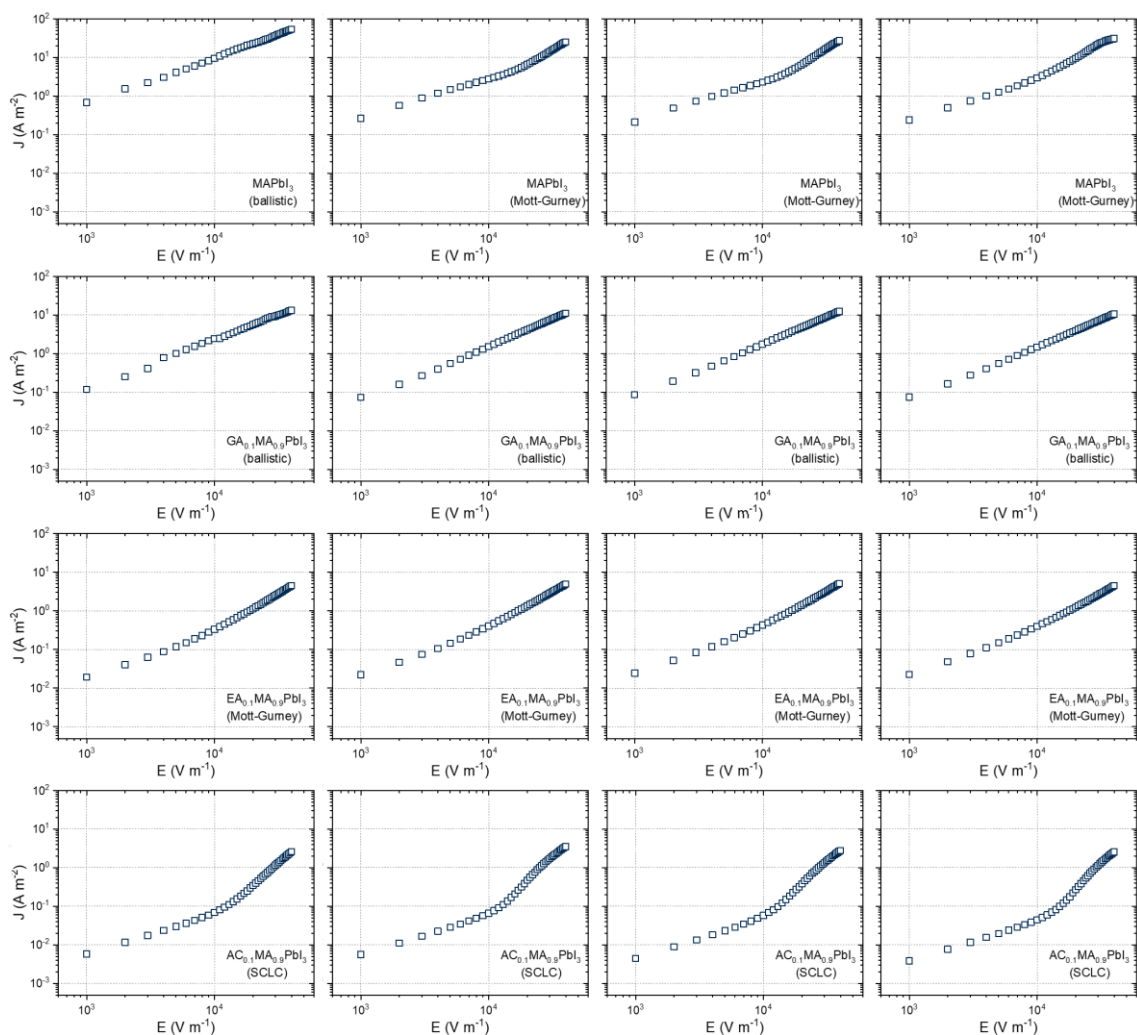


Figure S7 - Four forward measurements with a scan rate of 0.5 V s^{-1} used to evaluate the electronic carrier in samples of each composition.

Supplementary Note 9: Frequency-dependent dielectric permittivity

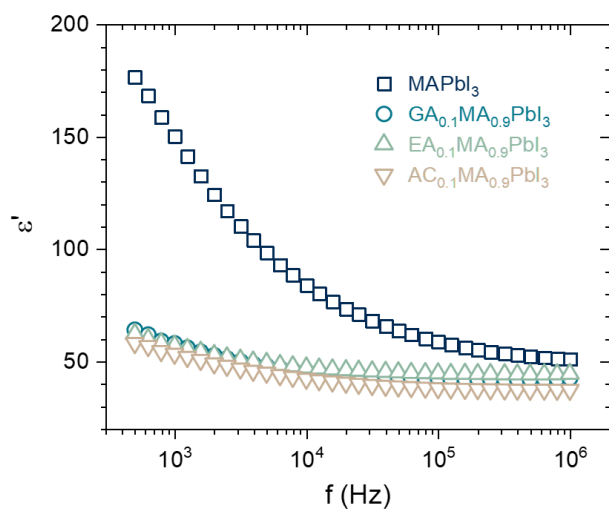


Figure S8 - Real part of the dielectric permittivity as a function of frequency measured from $5 \cdot 10^2$ to 10^6 Hz at room temperature.

Supplementary Note 10: Electronic carrier parameters

Table S3 - Summary of experimental data, models used, and evaluated electronic charge carrier parameters of samples. The n_e values were calculated using the relation $\sigma_{ohmic} = q\mu_e n_e$.

Composition	ϵ' (at 1 MHz)	σ_{ohmic} (10^{-6} S m^{-1})	Model	μ_e ($10^{-3} \text{ m}^2 \text{ V}^{-1} \text{ s}^{-1}$)	n_e (10^{16} m^{-3})
MAPbI ₃	51	784	Ballistic	60	8.1
		294	Mott-Gurney	17	11
		243	Mott-Gurney	19	8.0
		251	Mott-Gurney	30	5.2
GA0.1	42	183	Ballistic	24	4.8
		101	Ballistic	19	3.3
		120	Ballistic	21	3.5
		102	Ballistic	18	3.5
EA0.1	44	22.4	Mott-Gurney	3.0	4.6
		27.0	Mott-Gurney	3.4	5.0
		29.8	Mott-Gurney	3.5	5.3
		28.0	Mott-Gurney	3.1	5.7
AC0.1	37	5.89	SCLC	1.8	2.0
		5.65	SCLC	2.7	1.3
		4.57	SCLC	1.9	1.5
		3.90	SCLC	1.7	1.4

Supplementary Note 11: Changes in precursor organic salts exposed to ambient air

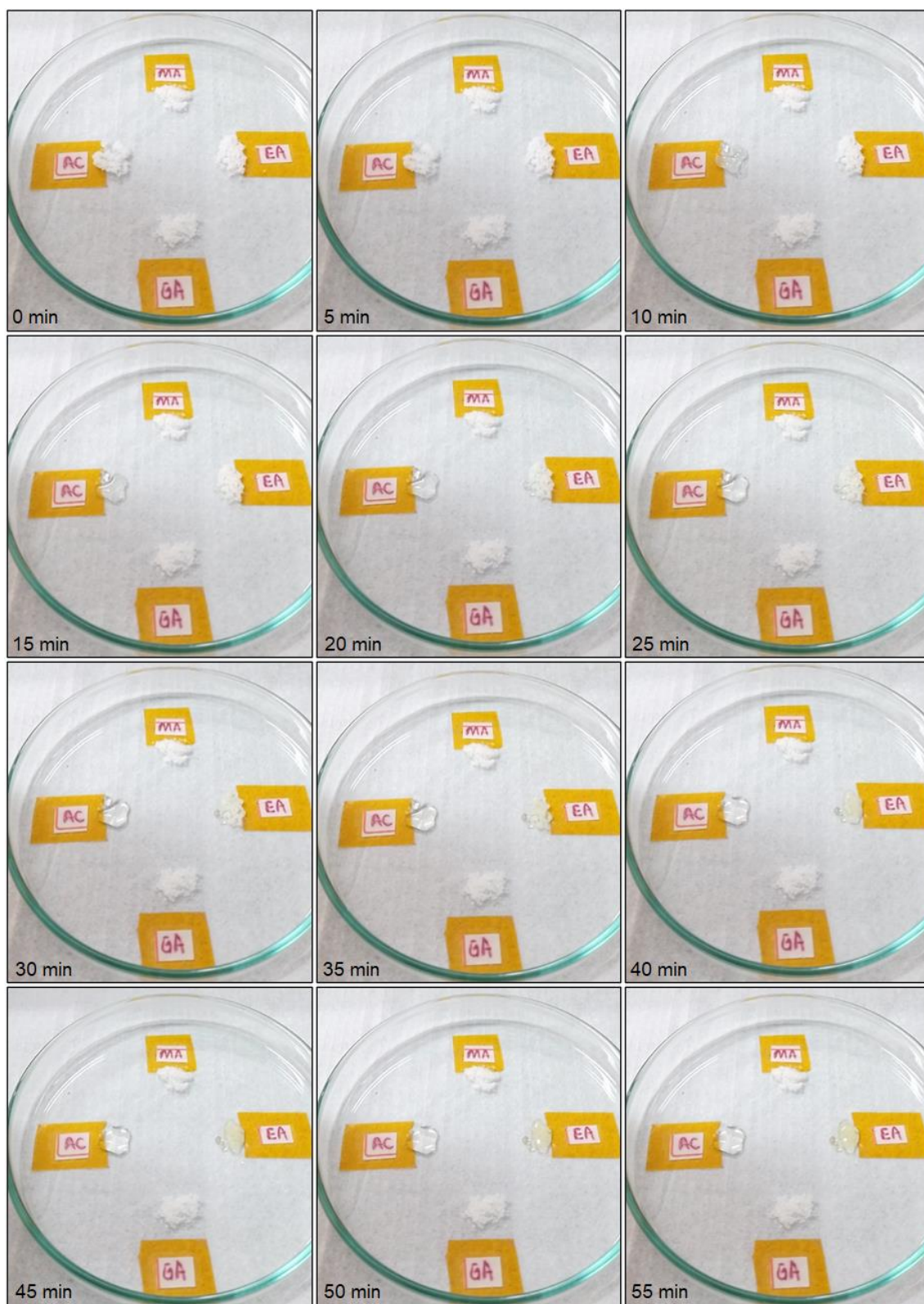


Figure S9 - Changes to visual aspect of portions of precursor MAI, EAI, GAI, and ACI powders with time when exposed to ambient air. MA, EA, GA, and AC are the positions of respective iodine salts. Tapes with the designation of organic cation salts are under the Petri dish.